

Highlights

The sensitivity of lowermost mantle anisotropy to past mantle convection

James Ward, Andrew M. Walker, Andy Nowacki, James Panton, Huw Davies

- Globally, anisotropy is well predicted by the present-day flow field only.
- On the regional (1000 km) scale, past mantle flow is likely observable in seismic anisotropy of the lowermost mantle in key areas.
- The sensitivity of anisotropy in post-perovskite-rich rocks to the past mantle flow correlates well with the time any given pocket of mantle spends within the post-perovskite stability field.

The sensitivity of lowermost mantle anisotropy to past mantle convection

James Ward^{a,1}, Andrew M. Walker^b, Andy Nowacki^{a,*}, James Panton^c, Huw Davies^c

^a*School of Earth and Environment, University of Leeds, Leeds, LS2 9JT, West Yorkshire, United Kingdom*

^b*Department of Earth Sciences, University of Oxford, Oxford, OX1 3AN, Oxfordshire, United Kingdom*

^c*School of Earth and Environmental Sciences, Cardiff University, Cardiff, CF10 3AT, Cardiff, United Kingdom*

Abstract

It is widely believed that seismic anisotropy in the lowermost mantle is caused by the flow-induced alignment of anisotropic crystals such as post-perovskite. What is unclear, however, is whether the anisotropy observations in the lowermost mantle hold information about past mantle flow, or if they only inform us about the present-day flow field. To investigate this, we compare the general and seismic anisotropy calculated using Earth-like mantle convection models where one has a time-varying flow, and another where the present-day flow is constant throughout time. To do this, we track a post-perovskite polycrystal through the flow fields and calculate texture development using the sampled strain rate and the visco-plastic self-consistent approach. As texture development also depends on the slip systems assumed, we compare the results of the flow fields under three ease-of-texturing slip system test cases. We compare the radial anisotropy parameters and the anisotropic components of the elastic tensors produced by the flow field test cases at the same location. We find, under all ease-of-texturing cases, the radial anisotropy is very similar (difference $< 2\%$) in the majority of locations and in some regions, the difference can be very large ($> 10\%$). The same is true when comparing the elastic tensors directly. Varying the ease-of-texture

*Corresponding author: a.nowacki@leeds.ac.uk

¹Now at HM Government Statistical Service

development in the crystal aggregate suggests that easier-to-texture material may hold a stronger signal from past flow than harder-to-texture material. Our results imply that broad-scale observations of seismic anisotropy such as those from seismic tomography, 1-D estimates and normal mode observations, will be mainly sensitive to present-day flow. Shear-wave splitting measurements, however, could hold information about past mantle flow. In general, mantle memory expressed in anisotropy may be dependent on path length in the post-perovskite stability field. Our work implies that, as knowledge of the exact causative mechanism of lowermost mantle anisotropy develops, we may be able to constrain both present-day and past mantle convection.

Keywords:

1. Introduction

Mantle convection has played a critical role in shaping the present-day surface environment and its evolution through time. It remains unclear, however, how mantle convection varies spatially and evolves, particularly in the lowermost mantle. Seismic anisotropy offers a unique probe into the convective patterns of the lowermost mantle and has been observed nearly ubiquitously in the enigmatic D'' region (e.g. Wookey et al., 2005; Cottaar and Romanowicz, 2013; Nowacki et al., 2010, 2011; Wolf et al., 2023a). As seismic anisotropy is widely believed to be caused by the gradual alignment of anisotropic crystals during mantle flow (Nowacki and Cottaar, 2021), it may hold information about past and present-day flow.

Several studies have shown the alignment of MgSiO₃ post-perovskite (ppv) crystals in D'' from flow-induced strain can cause an Earth-like anisotropy signal (e.g. Wenk et al., 2006; Walker et al., 2011; Wenk et al., 2011; Nowacki et al., 2013; Cottaar et al., 2014; Chandler et al., 2021). These studies calculate their anisotropy from the flow field in approximately the same way. Strain rates experienced along a path through a mantle flow field are measured and used to model texture development in a polycrystal of a particular composition such as MgSiO₃ post-perovskite (Hirose et al., 2015) or periclase (Park et al., 2022). This texture is then combined with single-crystal anisotropy elastic tensors to estimate the elastic tensor for the whole polycrystal at the end of the pathline. This modelling approach has been a powerful tool to investigate the cause and controls of anisotropy in the lowermost mantle. Some have used this to study anisotropy in local regions

25 where subducting material is impinging on the core-mantle boundary (Wenk
26 et al., 2011; Cottaar et al., 2014; McNamara et al., 2002, 2003). Others
27 aimed to produce a map of radial seismic anisotropy for comparison with
28 tomographic observations (Walker et al., 2011) and explored the effects of
29 topotaxy (Walker et al., 2018; Chandler et al., 2021). Other studies have
30 predicted the shear-wave splitting (Silver and Chan, 1991) signal from these
31 ppv textures to compare with real observations (Nowacki et al., 2013; Nowacki
32 and Cottaar, 2021). What remains an open question, however, is to what
33 extent seismic anisotropy in the lowermost mantle holds information about
34 past mantle flow, and it is this question we investigate here. In line with the
35 previous studies, we assume lowermost mantle anisotropy is caused by the
36 alignment of ppv crystals but other mechanisms such as melt inclusions or
37 layering can also cause seismic anisotropy.

38 Constraining the influence of past flow on present-day anisotropy will
39 allow us to better use anisotropy to constrain the Earth’s mantle convec-
40 tion. If anisotropy is mainly impacted by present-day flow, then current flow
41 may one day be inverted from seismic tomography. On the other hand, if
42 anisotropy is sensitive to past flow, then observations of anisotropy may of-
43 fer unique sensitivity to past mantle convection. To infer the sensitivity of
44 seismic anisotropy to past flow, we compare the anisotropy in D'' calculated
45 with two flow field test cases. In one case, we use the full dynamic flow
46 field history where the flow is allowed to vary with time. In the other case,
47 the present-day flow snapshot is kept constant throughout time. Note both
48 flow fields have the same present-day mantle convection pattern. Previous
49 studies differ in how the texture was generated from the flow fields. Wenk
50 et al. (2011) traced particles to keep track of strain rates experienced along a
51 pathline during forward modelling of the scenario in question such as a sub-
52 ducting slab impinging onto the core-mantle boundary. This approach has
53 the advantage of a higher flow field resolution than a global flow inversion
54 used by other studies (Walker et al., 2011). When tracing particles during
55 forward modelling the final locations of the particles can not be controlled,
56 leaving regions in the model unsampled. In contrast, when tracing the par-
57 ticles backwards in time the final location can be defined, but previously
58 this has required a time-invariant flow field (Walker et al., 2011). In our
59 approach, we get the best of both of these approaches; we use modern man-
60 tle convection simulations to create high-resolution global flow fields with
61 Earth-like parameters (Davies et al., 2012a) and have control over where we
62 measure the anisotropy by tracing particles back in time. For this study, a

63 sufficiently Earth-like mantle convection field will have realistic flow veloci-
64 ties, flow velocity gradients and temperatures in the lower mantle. As the
65 model we use has a surface plate motion model, a reasonable viscosity profile
66 and a reasonable core temperature, we argue this model is sufficient for this
67 study.

68 In line with previous studies (Walker et al., 2011; Nowacki et al., 2010;
69 Walker et al., 2018), we assume anisotropy is created in D'' by the crystal-
70 lographic alignment of MgSiO_3 post-perovskite as several studies have sug-
71 gested its presence and anisotropic nature (Merkel et al., 2007; Miyagi et al.,
72 2010; Hirose et al., 2015; Kuwayama et al., 2022). As anisotropy is affected
73 by both the strain rates sampled along the particle path and the slip systems
74 of the material being textured, the sensitivity of anisotropy to past flow is
75 also controlled by these mechanisms. Therefore, we not only vary the flow
76 field but also the slip systems of post-perovskite. We do this by varying the
77 ease-of-texturing of post-perovskite to infer its effect on the ‘memory’ of the
78 material.

79 Our results provide a conservative estimate of the extent to which past
80 flow is observable in seismic anisotropy. We find that global, present-day
81 mantle convection dominates anisotropic signal in D'' , but in many regions
82 past mantle flow is recorded. Therefore, localised observations such as shear-
83 wave splitting (Silver and Chan, 1991) and body wave waveform studies may
84 be able to discriminate between models of mantle convection history. Broader
85 scale observations such as from seismic tomography will mostly be sensitive
86 to present-day flow and could be used to invert for mantle flow.

87 2. Methods

88 This study aims to test the sensitivity of present-day anisotropy (the full
89 elastic tensor) to past mantle flow in D'' assuming it is caused by texturing
90 of post-perovskite-rich material. To test the memory of seismic anisotropy,
91 we use a fully-dynamic model of mantle convection and create an Earth-like
92 mantle flow field history (Section 2.1). From this, we create two flow field
93 cases: one where mantle flow changes with time and the other where the
94 flow at the present day is kept constant through time. Note the flowfield we
95 use as the ‘present-day’ flowfield is that at the end of the mantle convection
96 simulation. As anisotropy is also sensitive to slip systems of the material
97 being textured, the impact of past flow on present-day anisotropy may also
98 be affected by these slip systems. Therefore, we also vary the slip systems of

99 post-perovskite and create three ease-of-texturing test cases. The resulting
100 anisotropy is analysed to determine the effect of past flow on present-day
101 anisotropy and whether an easily textured material dampens or enhances
102 this effect.

103 *2.1. Mantle convection model*

104 We use TERRA (Baumgardner, 1985; Bunge et al., 1997; Davies et al.,
105 2012b; Panton et al., 2023), a three-dimensional mantle convection code, to
106 solve the governing equations with the Boussinesq approximation and assume
107 an incompressible mantle (McKenzie et al., 1974). Driving parameters for
108 the simulation are listed in Table 1. The model domain is discretised into
109 129 radial layers with an average radial spacing of ~ 22.5 km. In each of
110 these layers, we form a grid by projecting a regular icosahedron projected
111 onto a sphere. The grid is equally discretised at each layer resulting in an
112 average lateral grid spacing of ~ 16 km at the core-mantle-boundary (CMB)
113 and ~ 30 km at the surface. The surface boundary is isothermal (300 K)
114 and has lateral velocities applied from plate motion reconstructions since
115 the beginning of the Neoproterozoic (Merdith et al., 2020). As such, the
116 model features hot ridges, plumes and cool subduction zones where surface
117 material is recycled into the mantle. The CMB boundary is also isothermal
118 (3000 K) and is free-slip. The CMB boundary temperature is lower than
119 current seismological and mineral physics estimates for CMB temperature
120 (Kim et al., 2020; Lobanov et al., 2021; Deschamps and Cobden, 2022) due
121 to the incompressible equation of state that we use. A theoretical adiabat
122 is added to account for compressibility when using the temperature field to
123 calculate post-perovskite stability. The adiabat is calculated using a linear
124 increase in temperature in the upper mantle (until 660 km depth) and then
125 fit to a quadratic increase in the lower mantle.

126 As well as heating from the bottom boundary, the model is internally
127 heated via the decay of radioactive isotopes, concentrations of which are
128 tracked using tracer particles. A depth and composition-dependent solidus
129 controls melting (van Heck et al., 2016), which occurs at ridges and plume
130 heads, causing heat-producing elements to be fractionated. We employ a
131 depth-dependent viscosity with a ~ 100 km thick lithosphere which is 100
132 times more viscous than the reference. Note that there is no temperature
133 dependence in the viscosity. Upper mantle viscosity is equal to the refer-
134 ence and a 30-fold jump in viscosity occurs across the bottom of the mantle
135 transition zone at 660 km depth (van Keken and Ballentine, 1998). Viscosity

Table 1: Driving parameters for the simulation. Reference viscosity is equal to the viscosity of the upper mantle.

Symbol	Parameter	Value	Unit
T_S	Surface temperature	300	K
T_{CMB}	CMB temperature	3000	K
η_0	Reference Viscosity	3×10^{21}	Pa s
ρ_0	Reference Density	4500	kg m ⁻³
k	Thermal conductivity	4	W m ⁻¹ K ⁻¹
α	Thermal expansivity	2.5×10^{-5}	K ⁻¹
C_p	Specific heat capacity	1100	J kg ⁻¹ K ⁻¹

136 drops off in the bottom 150 km of the mantle to simulate the drop in viscosity
 137 across the post-perovskite transitions which occur there (Li et al., 2014).

138 For the purposes of our study, it is important that we have features in
 139 our simulated mantle which are of a similar scale to those found in Earth.
 140 The mixed heating Rayleigh number for the simulation is 8.8×10^8 , which is
 141 in line with estimates for Earth’s mantle (Bunge et al., 1997). In our simu-
 142 lation, the mantle cools at a rate of 70 K Gyr⁻¹ which is in good agreement
 143 with estimates of Earth’s mantle cooling rate (Labrosse and Jaupart, 2007).
 144 At the present day, the surface heat flux in the model is 40.5 TW, only
 145 slightly higher than current estimates for Earth’s mantle heat flux (Davies
 146 and Davies, 2010). All of this gives us confidence that our simulation is
 147 thermally behaving in a similar way to the Earth and so should produce
 148 thermal features which are recognisably Earth-like. Figure 1 shows the tem-
 149 perature and radial flow fields in the lower mantle as well as the predicted
 150 post-perovskite thickness. Although Earth-like, it is unlikely that this model
 151 will perfectly capture the finest properties of mantle convection. As we are
 152 comparing the flow field models to each other, a mantle convection model
 153 with the properties described above is suitable for our purposes.

154 2.2. Predicting anisotropy from flow fields

155 We calculate anisotropy in the lowermost mantle from the flow fields in a
 156 similar way to Walker et al. (2011) with the addition of allowing for a time-
 157 varying flow field. We give a brief summary of the methodology and explain
 158 the addition of a time-varying flow field.

159 The flow field is taken from the mantle convection model outlined in Sec-
 160 tion 2.1. For each point of interest, we trace a particle backwards through

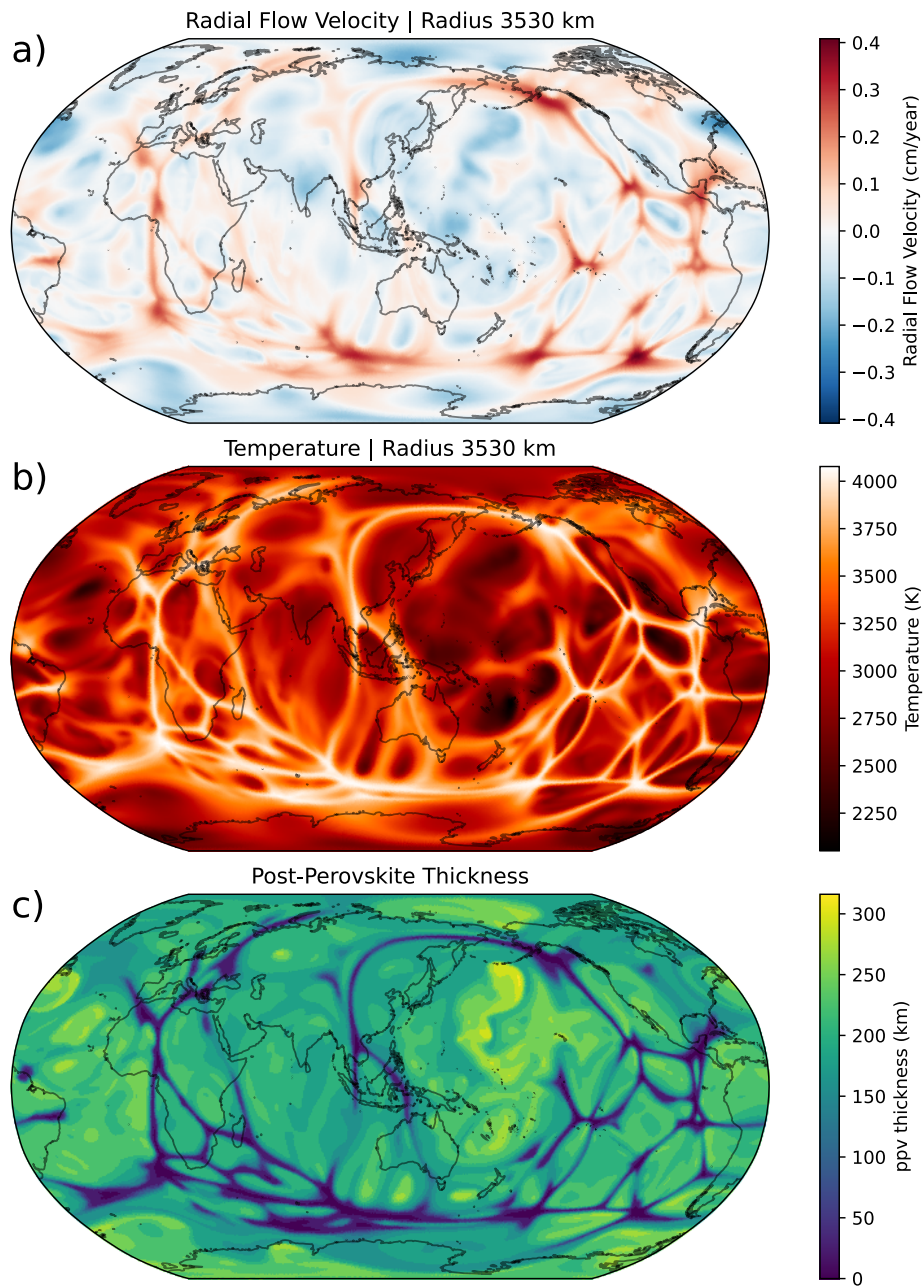


Figure 1: Present-day (end of mantle convection simulation, 0 Ma) summary snapshot of the mantle convection model used in this study showing (a) radial flow velocity, (b) temperature (with adiabat added), and (c) post-perovskite thickness. Notice that upwelling, high-temperature regions also have very thin or no post-perovskite and mark areas of convergent flow.

161 time in the flow field using 4th-order Runge-Kutta integration with a con-
162 stant time step of 25,000 years. This timestep gives very similar results
163 to that of a time step of 5000 years. Note that for a time-constant flow
164 field, we will be tracing streamlines through the final flow field snapshot
165 whereas in the time-varying case, we will be tracing path lines using multiple
166 flow field time snapshots. The particle continues to be traced back through
167 time until it reaches the phase transition between post-perovskite and per-
168 ovskite. Whether there is a phase transition at that location is determined
169 using the pressure and temperature at the location and a Clapeyron slope
170 of $7.0 \times 10^{-3} \text{ MPa K}^{-1}$ and pressure intercept of 105.7 GPa. The predicted
171 post-perovskite thickness in the model is shown in Figure 1c. The pressure
172 is calculated using the density from 1-D Earth model ak135 (Kennett et al.,
173 1995) and temperature from the model's temperature field.

174 At each step along the path, we extract the velocity gradient tensor and
175 use this to calculate the textural evolution of a post-perovskite polycrystal.
176 The evolution of the polycrystal needs to model the rotation and alignment
177 of all the crystals in the aggregate. Rather than describing all interaction
178 between adjacent crystals, we use the visco-plastic self-consistent (VPSC)
179 approach (Lebensohn and Tomé, 1993). VPSC represents adjacent grain
180 interactions by embedding each grain in a homogeneous medium which rep-
181 represents the other grains in the polycrystal. For the velocity gradients to be
182 translated to the rotation and deformation of the polycrystal, we assume
183 material properties of post-perovskite in the form of slip system activities.
184 The slip systems impact the texture development along the path and also
185 the final anisotropy. Therefore, to investigate the influence of past flow on
186 anisotropy, we need to investigate the effect of different slip systems. This
187 is done by varying the slip system activities such that the ease of texture
188 development is varied.

189 To calculate the texture, we use 500 post-perovskite crystals which are
190 randomly oriented at the beginning of each path. At the end of the pathline,
191 the crystals have been rotated. From these orientations, we calculate the
192 elastic tensor of the polycrystal by computing the Voigt-Reuss-Hill average
193 over all crystal orientations and the single-crystal elastic tensor. Here, we use
194 single-crystal properties found by Stackhouse et al. (2005) and Stackhouse
195 and Brodholt (2007) interpolated in pressure-temperature space with the
196 approach described by Ammann et al. (2010) using pressure derivatives from
197 Wentzcovitch et al. (2006). We assume the effect of different pressure and
198 temperature on the single-crystal anisotropy is small relative to other actors

199 in the model affecting the anisotropy such as the flowfield or slip system
200 activities in line with previous studies (Walker et al., 2011). From this elastic
201 tensor, the radial anisotropy parameters $\xi = V_{SH}^2/V_{SV}^2$ and $\phi = V_{PV}^2/V_{PH}^2$
202 can be calculated and compared. Alternatively, the elastic tensors between
203 the time-constant and time-varying cases can be compared directly. This
204 approach means the final anisotropy is an accumulation of texturing along
205 the whole path but, crucially, the importance of past texturing is uncertain.

206 To allow the flow field to vary with time, we take flow field snapshots at
207 10 Ma intervals and linearly interpolate between them for intervening times.
208 We use 4th-order Runge-Kutta integration to find the new location of the
209 particle based on the flow velocities at its current location and time. The
210 spatial gradient of the flow field is calculated and a new particle location is
211 found using the time-interpolated flow field. This process is repeated until the
212 particle reaches the phase transition from post-perovskite to perovskite. Note
213 that because the particle is being traced until it hits this phase transition,
214 the time each particle travels will be very different with the longest paths
215 have the particles travelling for 120 Ma. If the final location of the particle
216 is not in the post-perovskite stability field, no anisotropy is calculated and
217 plotted in grey later in Section 3.

218 *2.3. Test setup*

219 To explore the dependence of present-day anisotropy on past mantle flow,
220 we perform the texture development calculation described above on an equal-
221 area grid approximately 50 km above the core-mantle boundary. The grid
222 was created using the healpix algorithm (Gorski et al., 2005). The resulting
223 anisotropy, and therefore its sensitivity to past flow, is controlled both by
224 the strain rates sampled along the path and the slip system activities of the
225 material being textured.

226 We use the flow field from the model described in Section 2.1 and perform
227 the analysis in two cases. In the first case, the flow field is time-constant and
228 we trace particles as streamlines through the present-day flow field. In the
229 other case, the flow field is time-varying and we trace the particles as path
230 lines through the whole dynamic history. We use the present-day flow as
231 the constant-through-time case because it is common for seismic anisotropy
232 observations to be interpreted in the context of present-day flow only. To
233 predict elastic anisotropy, we need to assume the ppv slip system activities
234 which can impact the final anisotropy and therefore the impact of past flow
235 on such anisotropy. We use three slip system cases where we vary how easily

Slip System	Ease of texture development		
	Hard	Medium	Easy
[100](110)	1	1	1
[010](001)	1	1	1
[001](100)	3	5	10
[010](100)	3	5	10
[001]{110}	3	5	10
$\langle 110 \rangle (001)$	2	2	2
$\langle 110 \rangle \{110\}$	3	5	10

Table 2: Table showing the relative critical resolved shear stress (CRSS) coefficients used in VPSC for the different ease-of-texture cases. Each of these accommodates strain along the 001 plane as observed by Miyagi et al. (2010). The different models represent different scenarios for how easily texture develops in the post-perovskite polycrystal. Slip systems with infinite CRSS cannot accommodate strain.

236 the ppv aggregate develops texture and allow the texture to develop on the
237 001 plane. The slip systems activities are listed in Table 2.

238 We first analyse differences between the flow fields using summary statis-
239 tics of the paths such as path length and path tortuosity. This shows the
240 difference a time-varying flow field can have on the paths and the sampled
241 strain rates. Then, we compare the anisotropy outputs between the flow fields
242 for each of the ease-of-texturing scenarios. We do this both in terms of radial
243 anisotropy parameters ξ and ϕ and the anisotropic components of the elastic
244 tensor to infer the relative impacts on different observations. At present,
245 lower mantle radial anisotropy is still challenging to constrain accurately
246 with seismic tomography (Chang et al., 2014). Future tomography models
247 may provide useful broad-scale observations of lowermost mantle anisotropy,
248 therefore it is important to know if these observations are impacted by past
249 mantle flow. Before calculating the misfit between elastic tensors, we remove
250 the isotropic component (Browaeyns and Chevrot, 2004) as we only want to
251 compare the difference in anisotropy. We calculate the misfit with

$$\text{misfit} = \sqrt{\sum_{ij} (C_{ij}^{tv} - C_{ij}^{tc})^2}, \quad (1)$$

252 where C_{ij}^{tv} is the elastic tensor produced by the time-varying flow field and
253 C_{ij}^{tc} is the time-constant flow field. We use Voigt matrix representations of
254 the elastic tensors (a 6×6 matrix) where ij are the indices of the matrix

255 notation we use. From the misfits for each texturing scenario, we can infer
256 the influence of past flow on present-day anisotropy, the impact of ease-of-
257 texturing, and what controls the size of the misfit.

258 **3. Results and interpretation**

259 In this section, we first compare the path length and path tortuosity
260 to analyse the effect a time-varying flow field can have on particle paths.
261 Then, for each of the ease-of-texturing scenarios, we compare the anisotropy
262 between the flow field scenarios. To compare the anisotropy, we analyse
263 the difference between the anisotropic components of the elastic tensors to
264 infer the impact of past flow on measurements that are sensitive to different
265 parts of the elastic tensor such as shear-wave splitting. Then, we use the
266 radial seismic anisotropy values to infer the sensitivity of seismic tomography
267 observations to past mantle flow.

268 *3.1. Path differences*

269 The paths taken by particles through a flow field have a direct impact on
270 the anisotropy at the end of the path. If the path line through a time-varying
271 flow field is different to a streamline through the present-day flowfield, it mo-
272 tivates exploring whether the anisotropy is also different. Here, we explore
273 how different, if at all, the path properties are between the different flow
274 field cases. The properties we compare are the total path length and the
275 tortuosity. Tortuosity is defined as a ratio between the path length and the
276 linear distance between the start and end points of the path. Essentially it is
277 a measure of how non-linear the path is. Figure 2 shows the path length in
278 the time-constant and time-varying cases as well as their difference. It shows,
279 for the majority of locations, the path lengths are very similar (<500 km).
280 In some regions, a time-varying flow field can lead to significantly longer or
281 shorter paths with some differences going up to 6000 km. Analysing the tor-
282 tuosity tells a similar story (Figure 3) with the majority of locations showing
283 negligible differences and some locations having very large differences. The
284 difference in tortuosity shows that not only are the paths longer or shorter
285 but also that the linearity of the paths changes. This comparison shows that
286 a time-varying flow field can significantly affect the paths taken by parti-
287 cles. In the next section, we present the differences in general and seismic
288 anisotropy for the different flow fields.

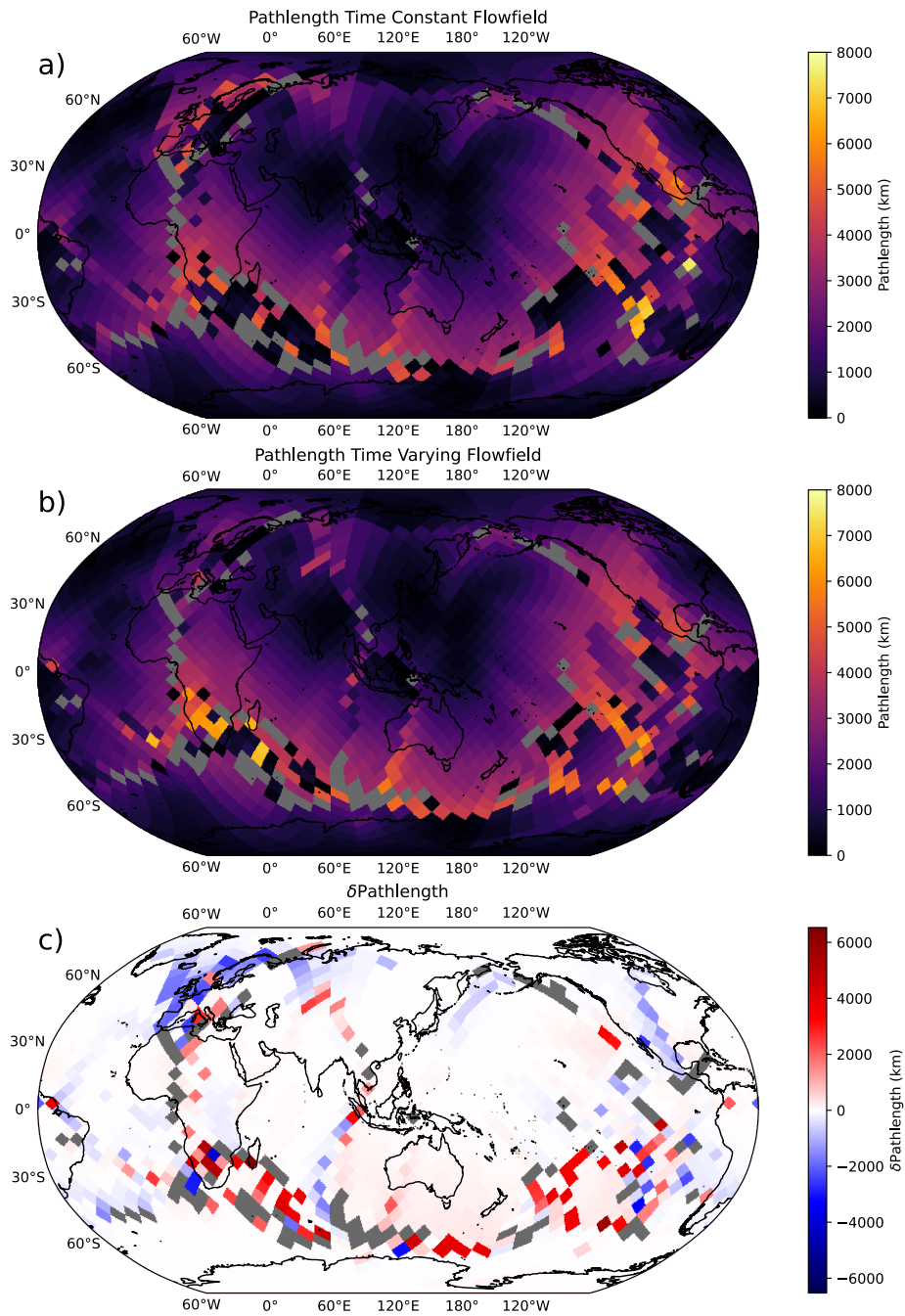


Figure 2: Maps comparing the path lengths in the ppv stability field ending at each location at 3530 km radius for (a) the time-constant flow field, (b) time-varying flow field and (c) the difference in the length of paths.

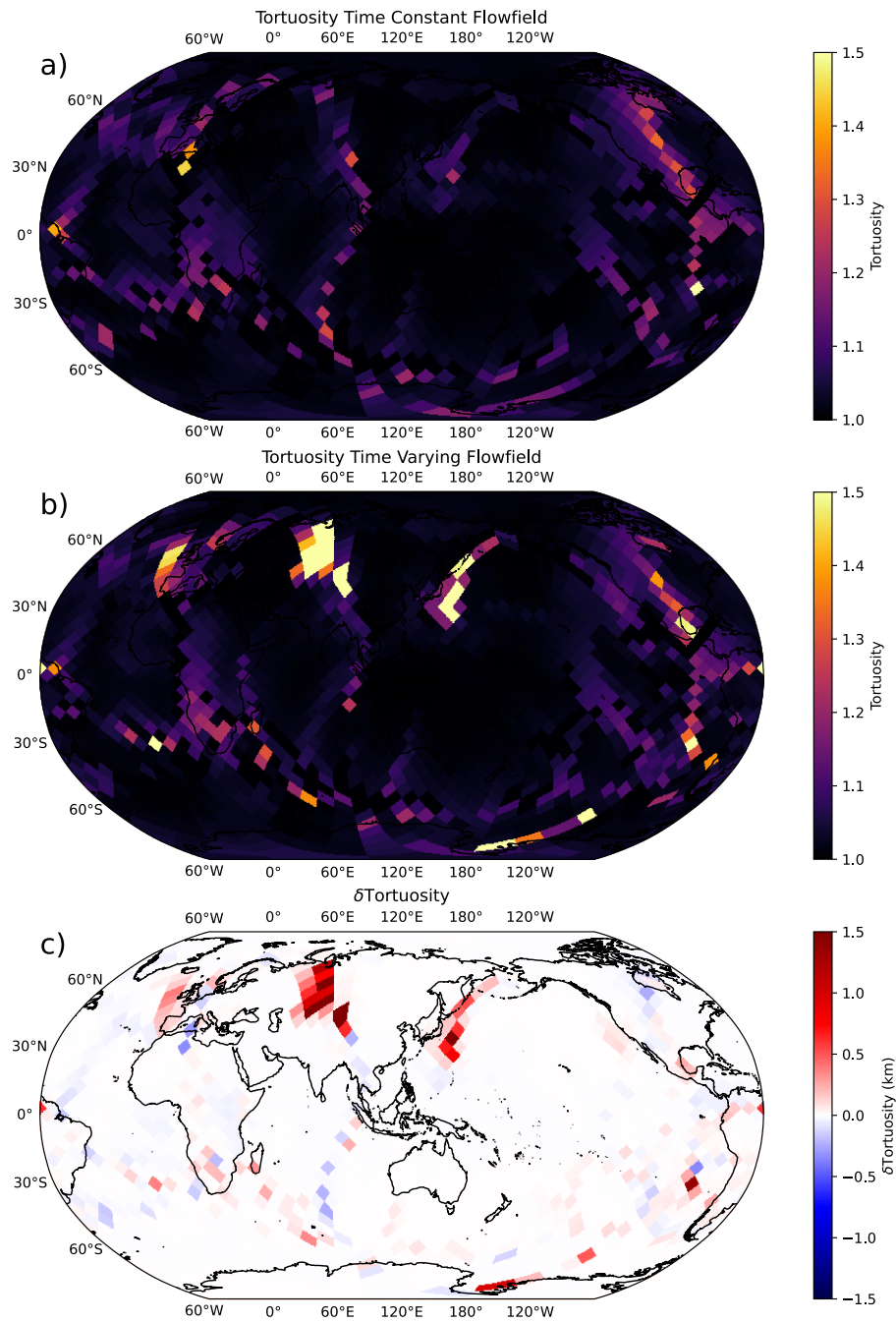


Figure 3: Maps comparing the tortuosity in the ppv stability field ending at each location at 3530 km radius for (a) the time-constant flow field, (b) time-varying flow field and (c) the difference in the length of paths.

289 *3.2. Anisotropy comparison*

290 As shown, a time-varying flow field can significantly alter the paths of
291 particles. To predict the anisotropy from these paths, we need to assume the
292 slip system activities of ppv which may also impact the sensitivity of such
293 anisotropy to past flow. In this section, we investigate the spatial distribution
294 of the differences in general and radial anisotropy of the flow fields for each
295 of the ease-of-texturing models.

296 *3.2.1. General anisotropy*

297 As described in Section 2.3, we compare the general anisotropy between
298 the flow field test cases by taking the misfit between the elastic tensors at
299 the same locations. Figure 4 shows a map of the misfits for the three ease-of-
300 texturing cases. In the majority of locations, for all ease-of-texturing cases,
301 the difference is small (< 50 GPa), however, in some local regions, there
302 are very large differences (> 300 GPa). For context, a 50 GPa difference
303 is equivalent to the misfit between two ppv crystals with properties from
304 Stackhouse et al. (2005) where one is rotated by less than 15° around the b
305 axis. A 300 GPa difference is equivalent to comparing the two ppv crystals
306 where one is rotated by approximately 45° .

307 Visual inspection of Figures 2, 3, and 4 suggests a relationship between
308 the differential path measures earlier (path length and tortuosity) and gen-
309 eral anisotropy misfit. We quantitatively investigate this possible relation by
310 plotting the misfit and the path parameters and calculating the Spearman
311 correlation coefficient (Figure 5). We also investigate the possible contribu-
312 tion of temperature at the end of the path and the influence of past flow.

313 We find a positive correlation between the difference in path length and
314 the misfit values (0.54). The same is true for the difference in tortuosity
315 (0.55). This reinforces our suggestion that the differences in the paths con-
316 tribute to the differences in anisotropy between the flow fields. There is also
317 a weak but positive correlation between the misfits and temperature (0.27)
318 suggesting some relationship between hotter regions and the impact of past
319 flow exists, but it is not as important as differences in path properties. We
320 also test how predictable the differential anisotropy between time-varying
321 and time-constant flow fields is using only the path length (Figure 5d). We
322 find a positive correlation (0.49) between path length and misfit suggesting
323 the longer paths tend to also be more sensitive to past flow.

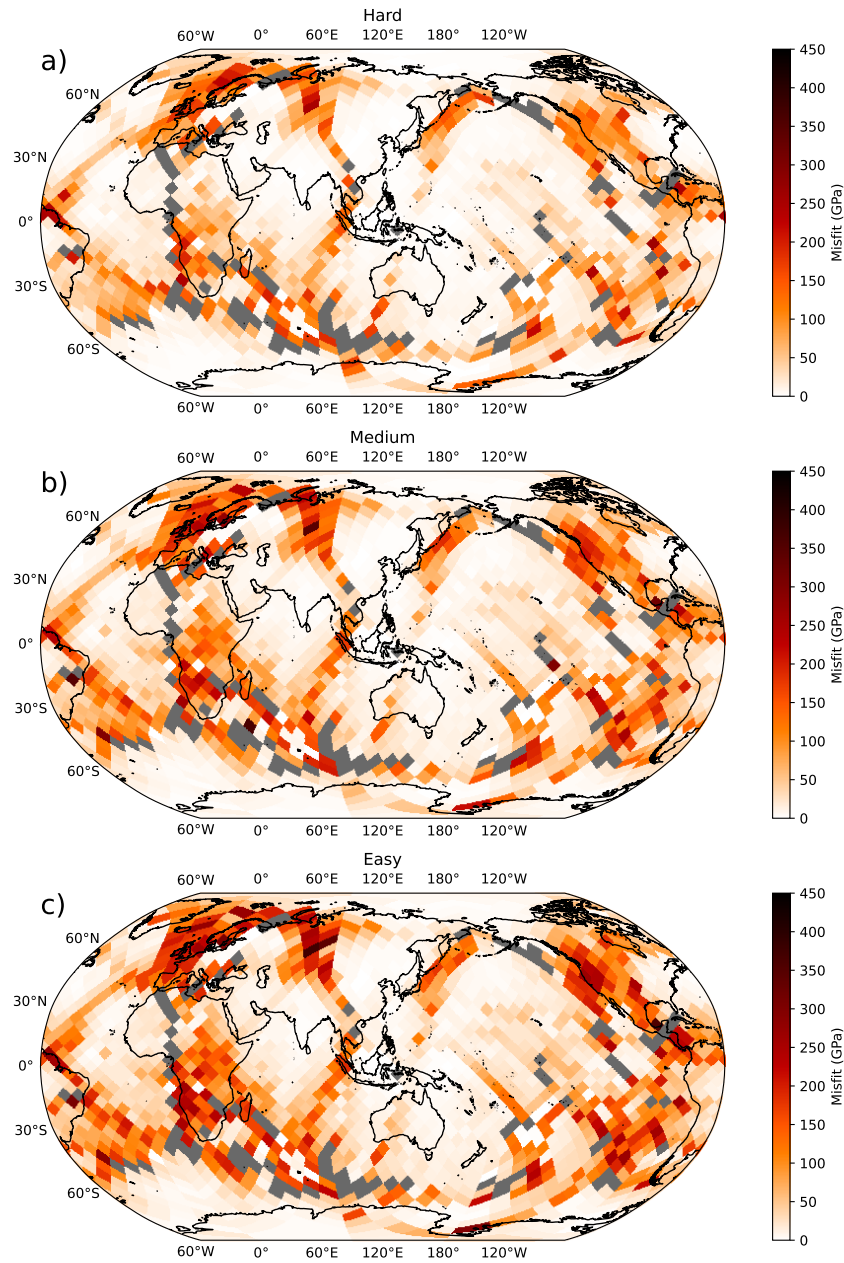


Figure 4: Maps showing the distribution of misfit values between the elastic tensors calculated with a time-constant and with a time-varying flow field for the three ease-of-texturing scenarios at 3530 km radius. The regions in grey show where post-perovskite is not stable. Notice the easier-to-texture case has more locations with a very high misfit (>350).

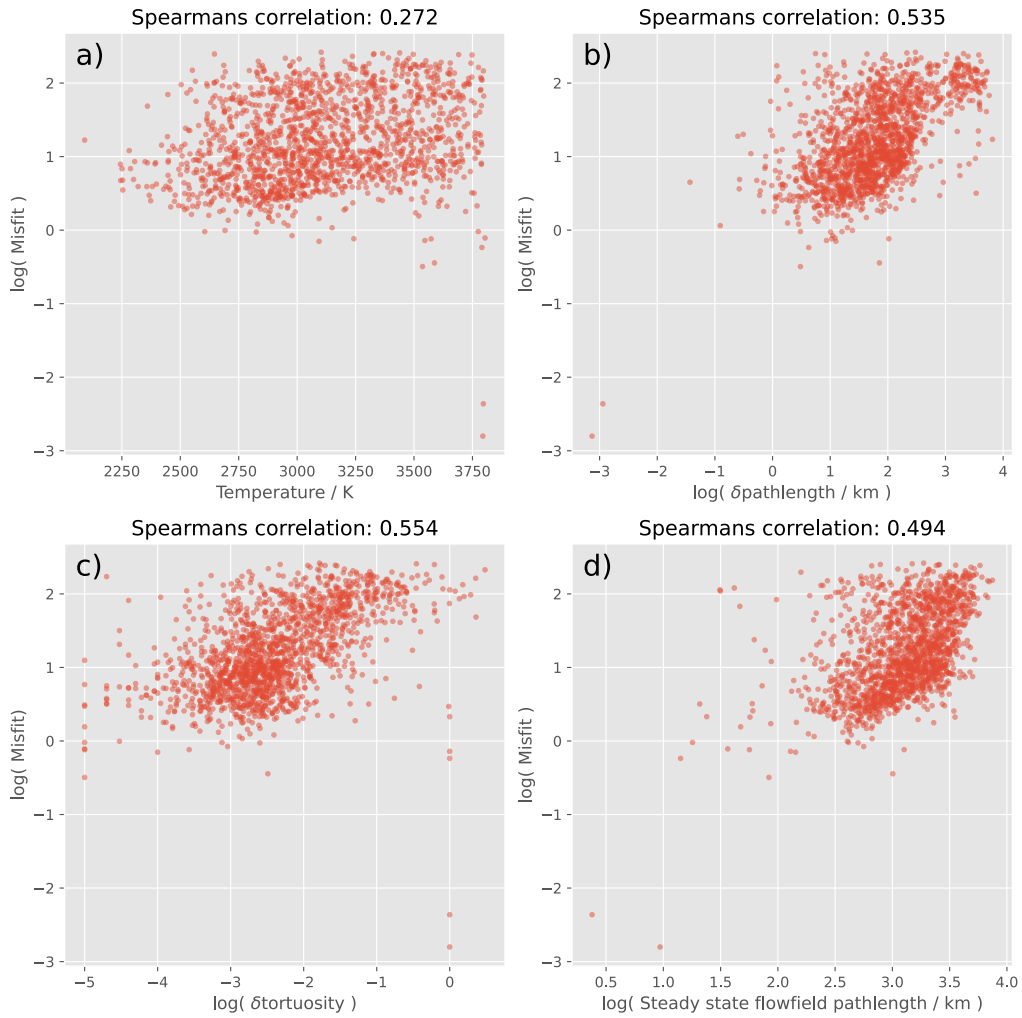


Figure 5: Scatter plots of the misfit between elastic tensors and parameters which may impact how much past flow affects the anisotropy at a location, for the hard-to-texture case. Panel (a) compares misfit with the temperature, (b) with the difference in path length, (c) with the difference in tortuosity, and (d) with the path length in the time-constant model. In panels (b), (c), and (d) we take the logarithm of the model parameters. The Spearman correlation value is shown in the title.

324 *3.2.2. Radial anisotropy*

325 In addition to comparing the elastic tensors directly, we compare the
326 radial seismic anisotropy predicted by the flow fields for the different ease-of-
327 texturing cases. We do this to test whether observations of radial anisotropy
328 such as those derived from seismic tomography hold information about past
329 flow. A map of the difference in radial anisotropy parameter ξ between
330 the flow models is shown in Figure 6 for each of the texturing cases. The
331 predicted S and P wave radial anisotropy for the flow field cases and their
332 differences for each ease-of-texturing case are shown in supplementary figures
333 A.10 to A.15. As with the general anisotropy, the majority of locations have
334 small differences ($< 1\%$), however, in some local regions, there are very large
335 differences ($> 10\%$). We define the percentage anisotropy as $(\xi - 1)\%$. As
336 with our interpretation of the general anisotropy, we hypothesise the large
337 differences are caused by differences in the particle paths (Figure 2). The
338 distribution of the difference in ϕ tells a similar story (see supplementary
339 Figure A.9).

340 The distributions of radial anisotropy for the flow fields are very similar
341 (Figure 7). Furthermore, the mean values are very similar where ξ has a dif-
342 ference of 0.14 % and ϕ a difference of 0.03 % for the hard-to-texture case
343 (Table 2). The distributions for the other ease of texturing cases show the
344 same pattern. Both the mean ξ ($\sim 2.8\%$) and ϕ ($\sim -7.3\%$) indicate horizon-
345 tally polarised P and S waves travel faster in D'' in our models. Because of the
346 free slip boundary condition, we expect flow near the core-mantle-boundary
347 to be near horizontal. This then textures the post-perovskite aggregate to
348 be broadly horizontal also for the 001 slip system and therefore, on average,
349 to cause horizontally polarised waves to travel faster.

350 The similar mean radial anisotropy in the models, in the context of the
351 spatial similarity also, suggests that in most of the lowermost mantle, radial
352 seismic anisotropy measurements are sensitive to present-day flow only.

353 *3.3. The effect of ease-of-texturing on past flow influence*

354 In addition to exploring the effects of particle path differences, we explore
355 how the ease of texturing of the crystal aggregate affects the impact of past
356 flow on present-day anisotropy. We do this by comparing the distributions of
357 the elastic tensor misfit (Section 3.2.1) between the ease-of-texturing cases.

358 In Figure 8a, we show the distribution of all the misfit values for each of
359 the three texturing cases. We observe the easy-to-texture case having larger
360 misfits than the hard-to-texture case suggesting sensitivity to time variations

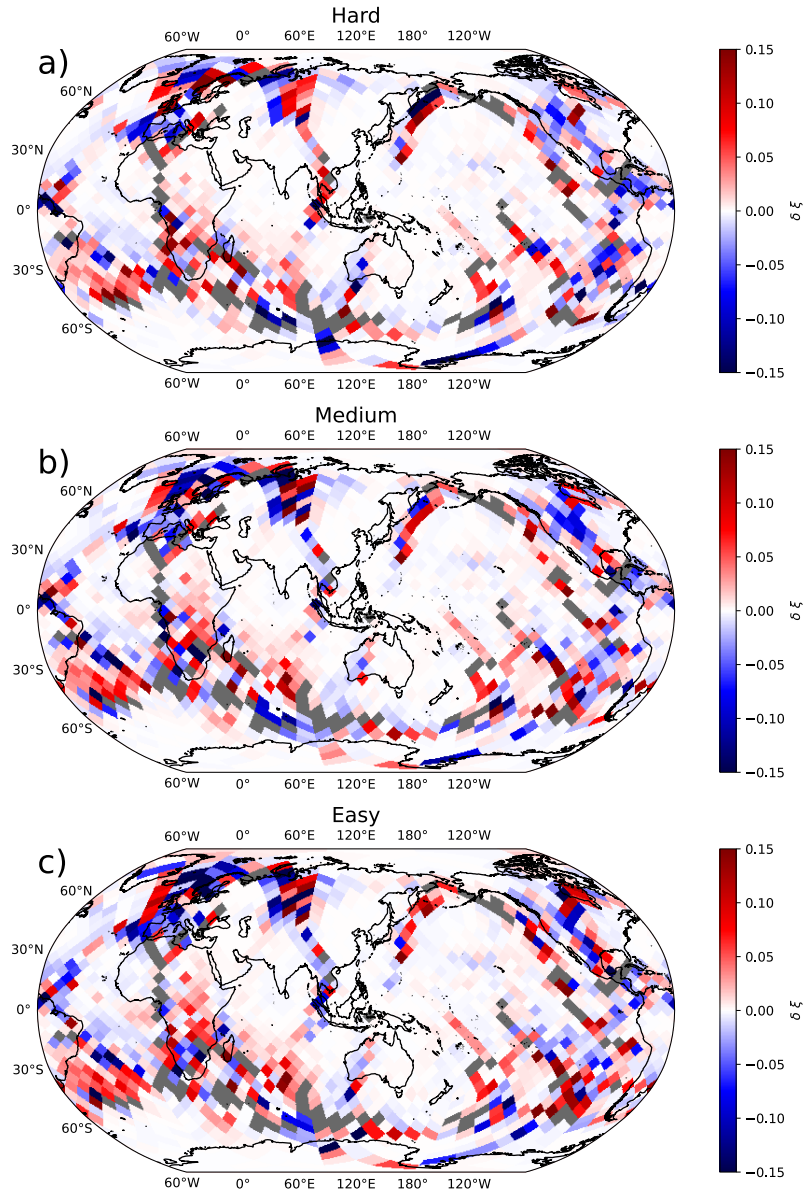


Figure 6: Maps showing the difference between shear-wave radial anisotropy at 3530 km radius (50 km above the core–mantle boundary) for the different flow fields with the different ease-of-texturing cases. The regions in grey show where post-perovskite is not predicted to be stable at this depth.

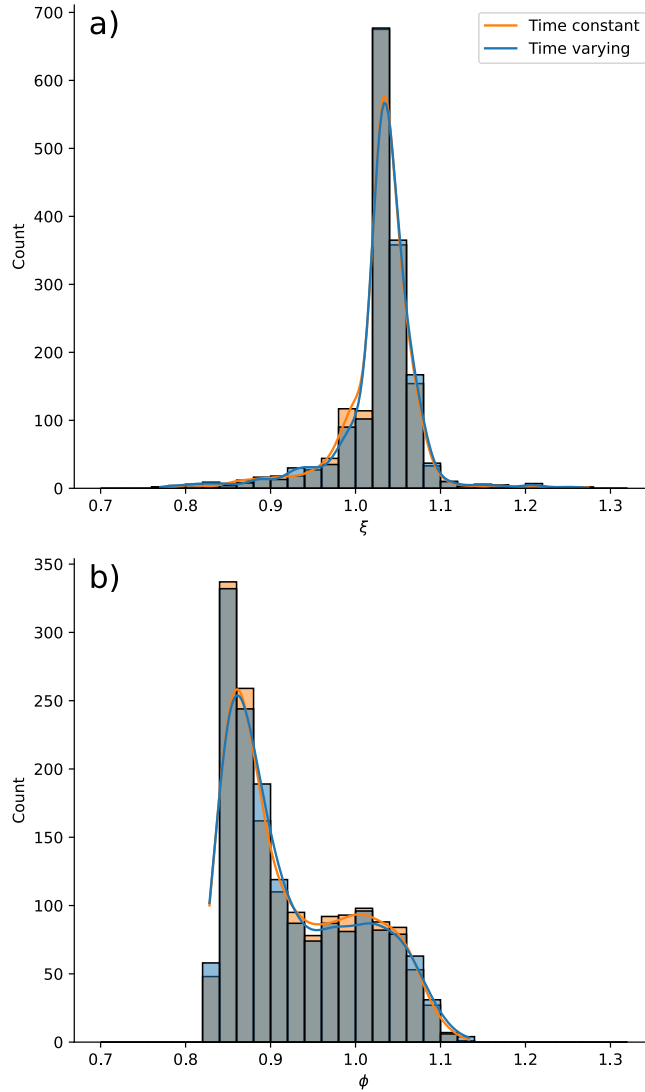


Figure 7: Histograms of S-wave (a) and P-wave (b) radial anisotropy coloured by whether the flow field was time-dependent or -independent. Here we can see very little difference between the two for either P- or S-wave radial anisotropy. The lines show the kernel density estimates for the distribution of radial anisotropy for the time-varying and time-constant cases. Note this is for the hard-to-texture case and other texturing cases show equally similar distributions between time-varying and time-constant flow fields.

361 in flow is affected by the material being textured. Specifically, an easy-to-
362 texture crystal aggregate will hold more texturing from past flow than a
363 hard-to-texture crystal aggregate. This is supported by Figure 8(b) where
364 there are significantly more misfits in the <10 GPa bin in the hard-to-texture
365 case. Analysing the radial anisotropy (see supplementary Figures A.16 and
366 A.17), shows the same pattern and therefore has the same implications for
367 interpreting observations such as seismic tomography.

368 We suggest easier-to-texture polycrystals hold more texturing from past
369 flow in our setup because of the difficulty to re-texture a heavily shear-
370 strained polycrystal. If the polycrystal experiences high strain rates early in
371 its path, an easy-to-texture material will be heavily textured and geometric
372 hardening, where the material hardness increases with plastic deformation
373 (Hansen et al., 2012; Mameri et al., 2019), will make new texturing more
374 difficult.

375 4. Discussion

376 As the previous sections show, for most locations in the lower mantle of an
377 Earth-like mantle convection model, seismic anisotropy is mostly sensitive to
378 the present-day flow field. In this section, we discuss the implications of these
379 results both for those making observations and also for those investigating
380 the material properties of post-perovskite. Then, we highlight limitations in
381 our modeling approach.

382 4.1. Implications for seismic anisotropy studies

383 We have shown in the majority of locations in the lower mantle, seismic
384 anisotropy is sensitive primarily to the present-day flow field, but in small
385 regions, the past flow has a strong influence. Therefore, the implications
386 our findings will have depend on the resolution and location of the seismic
387 anisotropy. Global-scale observations such as 1-D seismic anisotropy observa-
388 tions (De Wit and Trampert, 2015), current body-wave seismic tomography
389 (e.g. Simmons et al., 2021; Auer et al., 2014) or normal-mode observations
390 (Restelli et al., 2023) should be sensitive mainly to present-day flow only in
391 the lower mantle. Note that in the case of seismic tomography improvements
392 in resolution may lead to sensitivity to past flow. Regional-scale observations
393 from shear-wave splitting (e.g. Nowacki et al., 2010; Asplet et al., 2020; Wolf
394 et al., 2023a; Wookey et al., 2005) may be sensitive to present-day flow but
395 potentially could have information about past mantle flow. To investigate

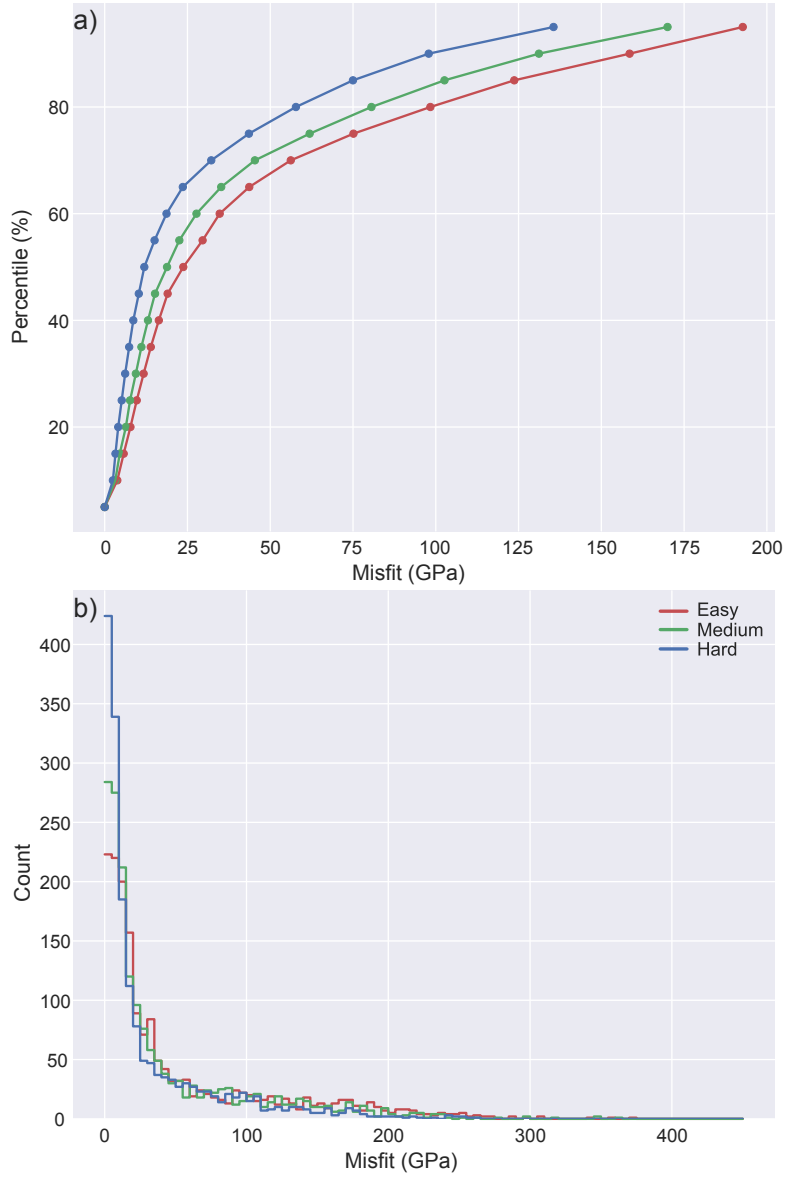


Figure 8: The effect of slip system activities on sensitivity to past flow. a) shows the different percentile misfit values coloured by the slip system label from Table 2. b) shows overlapping histograms for misfit data, also coloured by the slip system activities. The orange and blue lines are the kernel-density estimates for the time-constant and time-varying cases.

396 whether shear wave splitting observations have information about past flow,
397 future studies can compare the observations to those made from flowfield test
398 cases with time-varying and time-constant flowfields. This could potentially
399 constrain what historic flow was like. Future studies could also take existing
400 databases of splitting observations in D'' (e.g. Wolf et al., 2023b) and com-
401 pare them to predictions of different global flowfields to constrain what past
402 flow fields may have been like in the lower mantle.

403 We found a positive but weak correlation between temperature and elastic
404 tensor misfit (Figure 5), suggesting seismic anisotropy measurements in hot
405 regions may hold more information about past flow. We believe this weak
406 correlation is caused by differences in path lengths (Figure 2). The hot re-
407 gions have different path lengths because of the thin post-perovskite present.
408 Therefore, some paths may be very short and paths between the time-varying
409 and time-constant flowfields could be significantly different and have differ-
410 ent texturing history. Stronger correlations with other metrics such as path
411 length show multiple factors contribute to the sensitivity to past flow.

412 The longer paths in the time-constant flow field tend to also be more
413 affected by a time-varying flow field than the shorter paths (Figure 5). This
414 may be because there is more opportunity for the particle paths in the dif-
415 ferent flow fields to deviate, and thus the histories of strain rates likewise
416 tend to diverge. When interpreting regional observations such as those using
417 shear-wave splitting, it is most likely that a time-varying flow field must be
418 considered, with particular caution being taken with longer paths.

419 We have shown that to be able to interpret lower mantle seismic anisotropy
420 observations in terms of a time-varying flow field, it is vital to know how eas-
421 ily lowermost mantle minerals are textured. We found that harder-to-texture
422 crystal aggregates hold less information about past mantle flow than easier-
423 to-texture crystal aggregates.

424 *4.2. Modelling assumptions*

425 Our results suggest broad-scale observations of seismic anisotropy in the
426 lower mantle such as those from current seismic tomography or 1-D estimates
427 should be sensitive to present-day flow only. On the other hand, higher
428 resolution observations such as shear-wave splitting may hold information
429 about past flow depending on the region sampled. Our model setup is built
430 upon several assumptions and limitations which we discuss here.

431 A significant assumption we make is assuming deformation in D'' is ac-
432 commodated solely by dislocation creep everywhere. In lowermost mantle

433 conditions, it is likely that other deformation mechanisms are taking place
434 which may or may not result in the texturing of a crystal aggregate. It is
435 unclear what deformation mechanisms are present in the lower mantle, what
436 effect they have on texturing and where they occur. It is commonly believed
437 diffusion creep is present in hot regions, but whether this leads to texture
438 loss (McNamara et al., 2001, 2002), texture preservation (Wheeler, 2009)
439 or continued texture development (Dobson et al., 2019) is debated. Other
440 mechanisms such as pure dislocation climb creep (Boioli et al., 2017; Reali
441 et al., 2019) may be present and result in no texture development, but again,
442 where this happens in the lower mantle and what proportion of deformation
443 is accommodated by this remains uncertain. These will certainly affect the
444 sensitivity of seismic anisotropy to time-varying flow. Our approach means
445 we have essentially maximised the sensitivity of texturing to flow and there-
446 fore also maximised the influence of past flow. In light of this, our setup
447 maximises how much past flow influences present-day anisotropy observa-
448 tions. The likely effect of considering other deformation mechanisms is a
449 reduction in the time-sensitivity of seismic anisotropy. To properly account
450 for other deformation mechanisms, more information about the conditions
451 where they dominate and the effect they have on texturing is needed.

452 Another limitation is there is no cap on texture strength such as that
453 expected to occur from dynamic recrystallisation as dislocation density in-
454 creases. Not limiting texture strength in our model may lead to geometric
455 hardening where high CPO intensity becomes harder to texture further as
456 has been previously shown in olivine (Hansen et al., 2012; Mameri et al.,
457 2019), which could limit the formation of future texture. Capping texture
458 strength with some form of dynamic recrystallisation or in an ad-hoc way by
459 reducing the velocity gradient magnitude at each step along the path (e.g.
460 Wenk et al., 2011; Cottar and Romanowicz, 2013) most likely will reduce
461 the sensitivity to past flow and reduce the number of locations where there
462 are large differences between a time-constant and time-varying flow field. As
463 we observe differences between the flow field of up to 15 % radial anisotropy
464 we do not expect reducing the strain rates in an ad-hoc way will greatly
465 change our conclusions.

466 In our setup, we assume deformation occurs in pure post-perovskite and
467 there is no texture inheritance from deformation outside of the post-perovskite
468 stability field. Therefore, the particle path lengths and strain rates sampled
469 are affected by the Clapeyron slope and pressure intercept we chose. We used
470 a Clapeyron slope which is within the range of estimates from experiments

471 and calculations (Hirose et al., 2015; Kuwayama et al., 2022). By assuming
472 pure post-perovskite, we do not account for any additional phases such as
473 ferropericlasite or bridgmanite which may strengthen or weaken the anisotropy
474 depending on if and how texture may develop. Furthermore, effects such as
475 those from strain localisation are not accounted for.

476 5. Conclusion

477 We tested the sensitivity of present-day lowermost mantle anisotropy to
478 past mantle flow by comparing the anisotropy predicted from two mantle flow
479 field models: one where the flow field varies with time and another where
480 the flow is constant. As texture and anisotropy are controlled by both the
481 flow field and slip system activities we create three test cases where we vary
482 the ease-of-texturing to test for its impact. We find, in all ease-of-texturing
483 cases, low-resolution observations such as 1-D radial anisotropy observations
484 and seismic tomography are likely sensitive to present-day flow only. High-
485 resolution regional observations, such as those from shear-wave splitting, may
486 hold some information about past mantle flow. If the resolution of seismic
487 tomography improves, it may also have some sensitivity to past flow. Vary-
488 ing the ease-of-texturing of the crystal aggregate leads to a similar spatial
489 distribution but the easier-to-texture material leads to greater differences in
490 the anisotropy between the flow field cases at some locations. We investigate
491 what could contribute to the impact of past flow on present-day anisotropy.
492 We find path properties such as differences in path length and tortuosity
493 between the flow fields show the strongest correlation with anisotropy dif-
494 ference. We also find the temperature at the endpoint may also have an
495 effect with hotter temperatures leading to larger differences between the pre-
496 dicted anisotropy from a time-varying and constant flow field. From this, we
497 conclude there is no one dominant predictor of sensitivity to past flow. Ulti-
498 mately, we show that low-resolution observations of lower mantle anisotropy
499 such as those from current seismic tomography or 1D radial anisotropy esti-
500 mates are sensitive to present-day flow alone. This implies that inversions of
501 flow from such observations may give promising estimates of present-day con-
502 vection patterns. Regional, high-resolution observations such as those from
503 shear-wave splitting may provide some sensitivity to historic flow. As con-
504 straints on mineral physics and deformation mechanisms in D'' are tightened
505 in the future, our work gives us confidence that inversions for recent mantle
506 flow from seismic anisotropy observations may become possible in time.

507 **Acknowledgements**

508 JW, AW and AN are supported by NERC large grant Mantle Circu-
509 lation Constrained NE/T012684/1. JP and JHD are supported by NERC
510 large grant Mantle Circulation Constrained NE/T012633/1. AN is partly
511 funded by NERC standard grant NE/R001154/1 (REMIS: Reliable Earth-
512 quake Magnitudes for Induced Seismicity). Figures were made using Mat-
513 plotlib (Hunter, 2007) and cartopy (Met Office, 2010 - 2015). Code to perform
514 the seismic anisotropy calculation from flow is available upon request.

515 **Appendix A. Supplementary material**

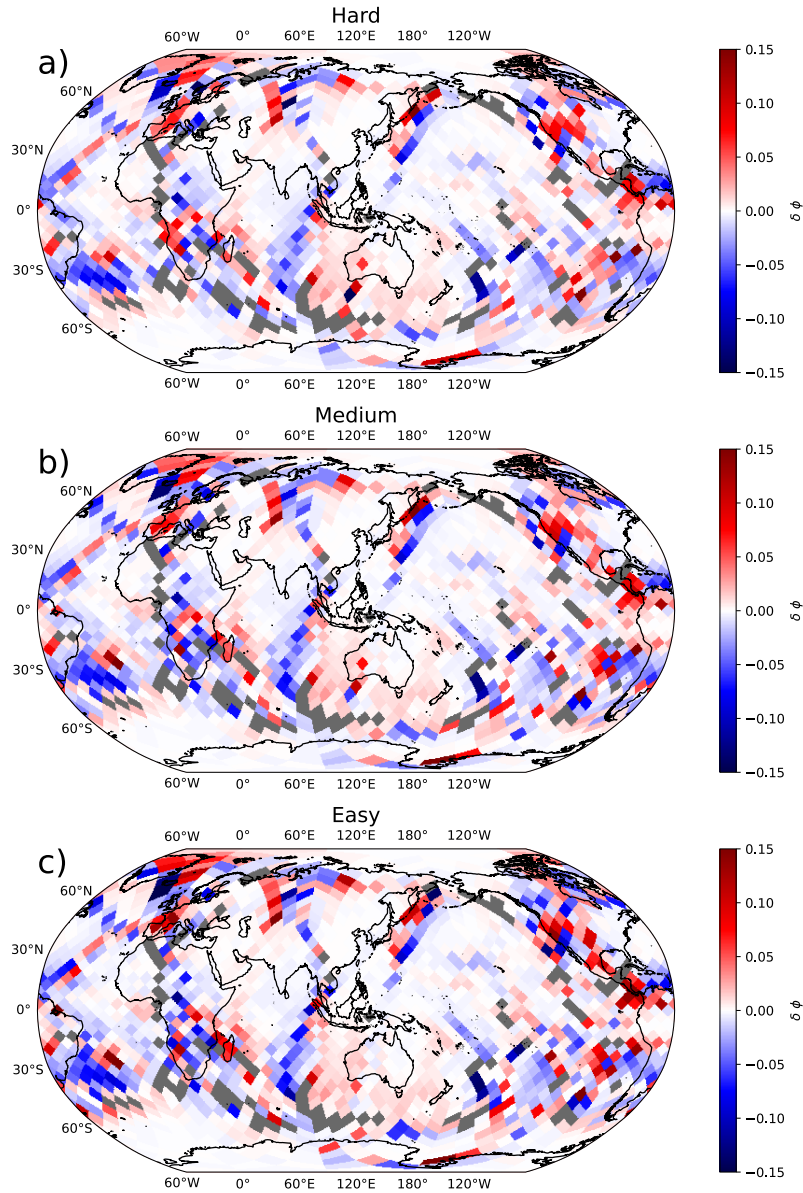


Figure A.9: Maps showing the difference between P-wave radial anisotropy (ϕ) at 3530 km radius (50 km above the core–mantle boundary) for the different flow fields with the different ease-of-texturing cases. The regions in grey show where post-perovskite is not predicted to be stable at this depth.

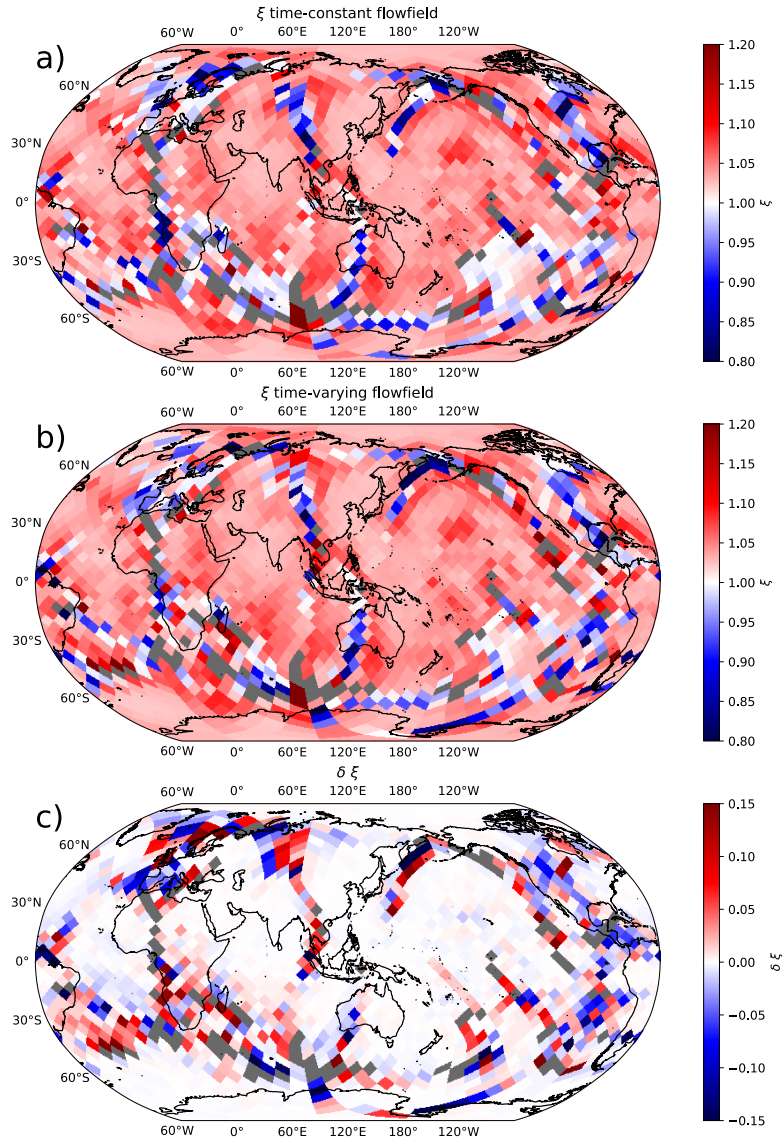


Figure A.10: Maps of S-wave radial anisotropy (ξ) at 3530 km radius (50 km above the core-mantle boundary) for the hard-to-texture case. We show ξ calculated with the time-constant flowfield (a), the time-varying flowfield (b) and the difference between the two (c).

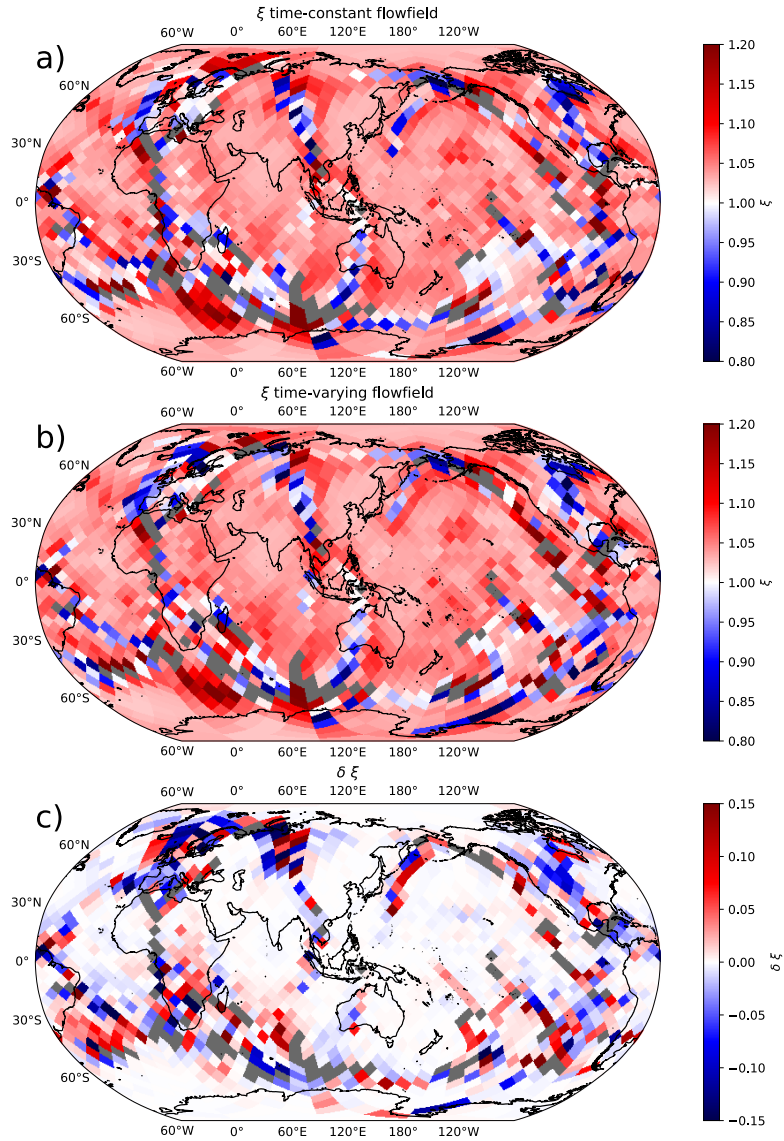


Figure A.11: Maps of S-wave radial anisotropy (ξ) at 3530 km radius (50 km above the core-mantle boundary) for the medium texture case. We show ξ calculated with the time-constant flowfield (a), the time-varying flowfield (b) and the difference between the two (c).

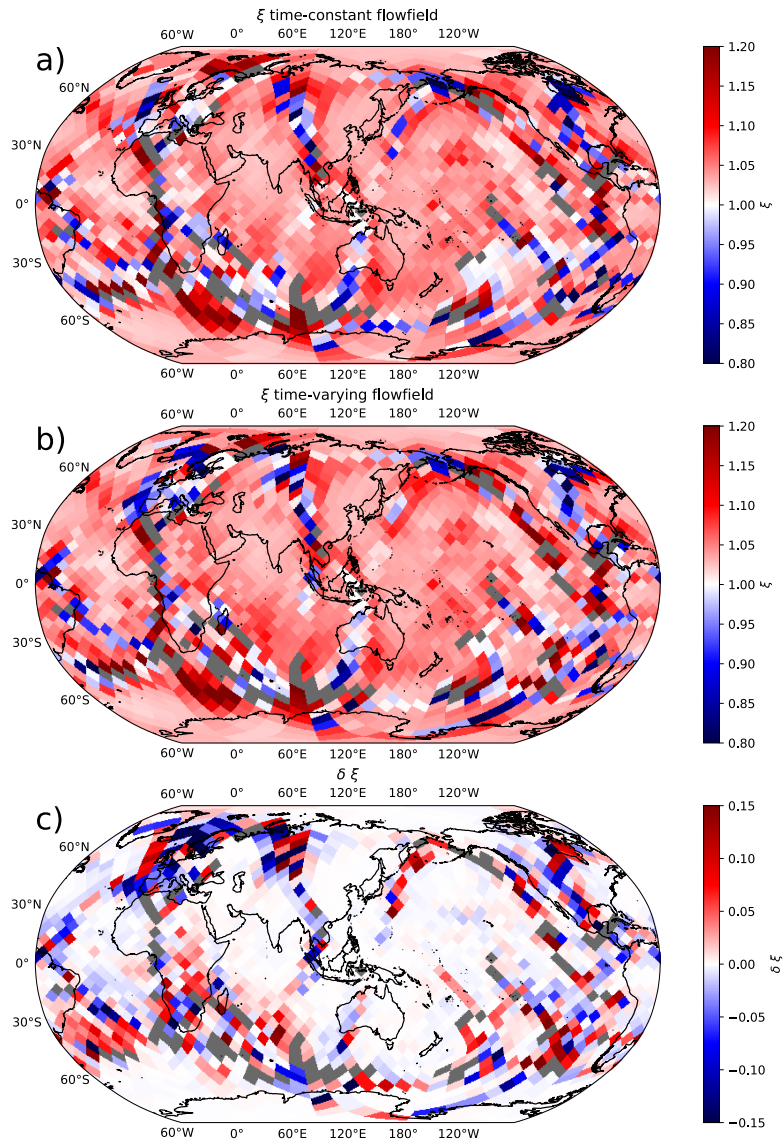


Figure A.12: Maps of S-wave radial anisotropy (ξ) at 3530 km radius (50 km above the core-mantle boundary) for the easy-to-texture case. We show ξ calculated with the time-constant flowfield (a), the time-varying flowfield (b) and the difference between the two (c).

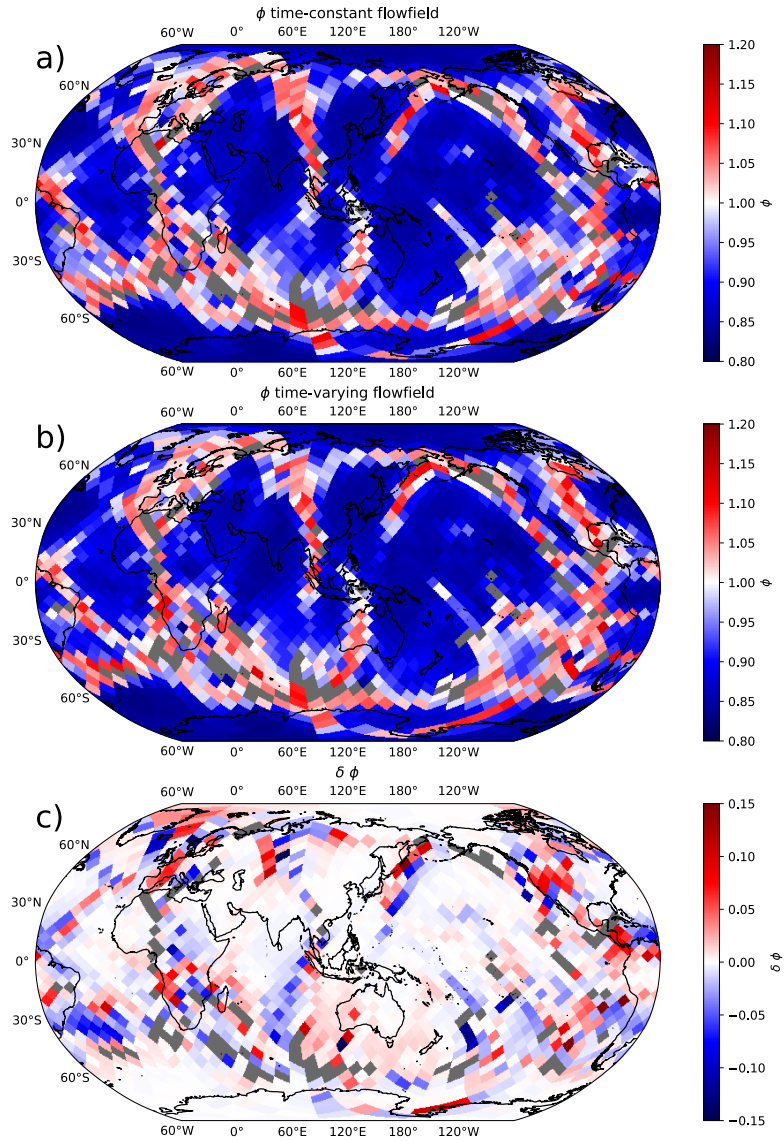


Figure A.13: Maps of P-wave radial anisotropy (ϕ) at 3530 km radius (50 km above the core-mantle boundary) for the hard-to-texture case. We show ϕ calculated with the time-constant flowfield (a), the time-varying flowfield (b) and the difference between the two (c).

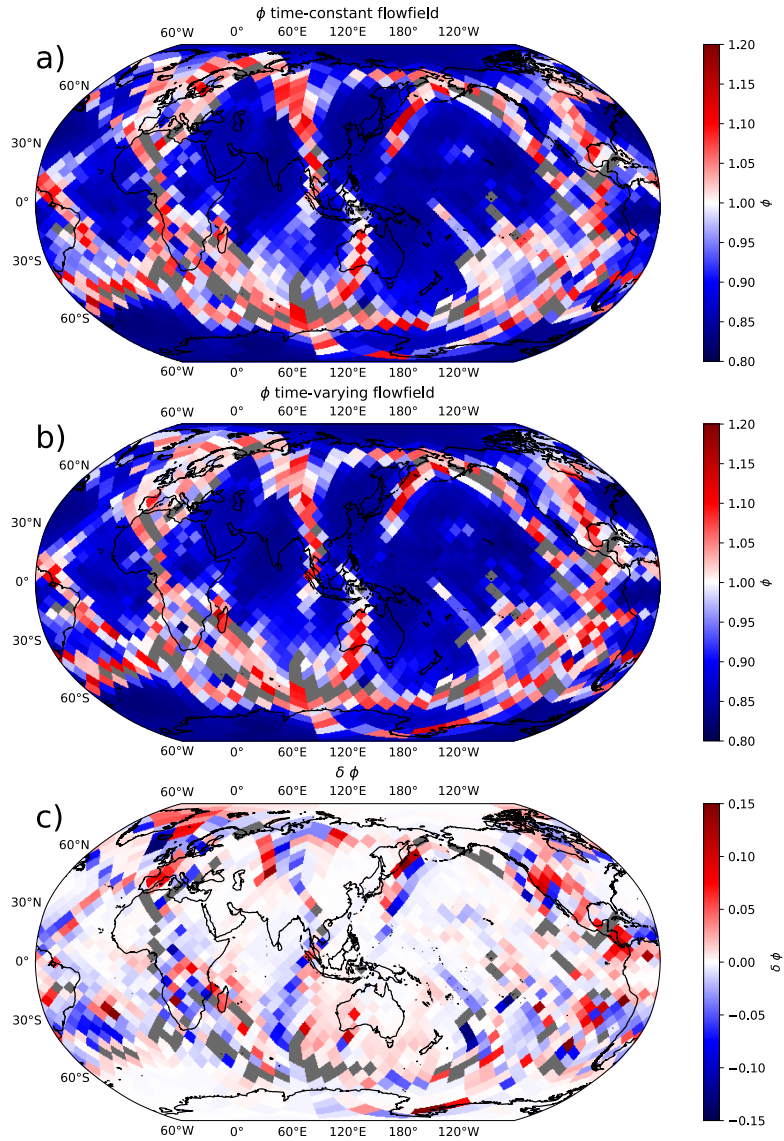


Figure A.14: Maps of P-wave radial anisotropy (ϕ) at 3530 km radius (50 km above the core-mantle boundary) for the medium texture case. We show ϕ calculated with the time-constant flowfield (a), the time-varying flowfield (b) and the difference between the two (c).

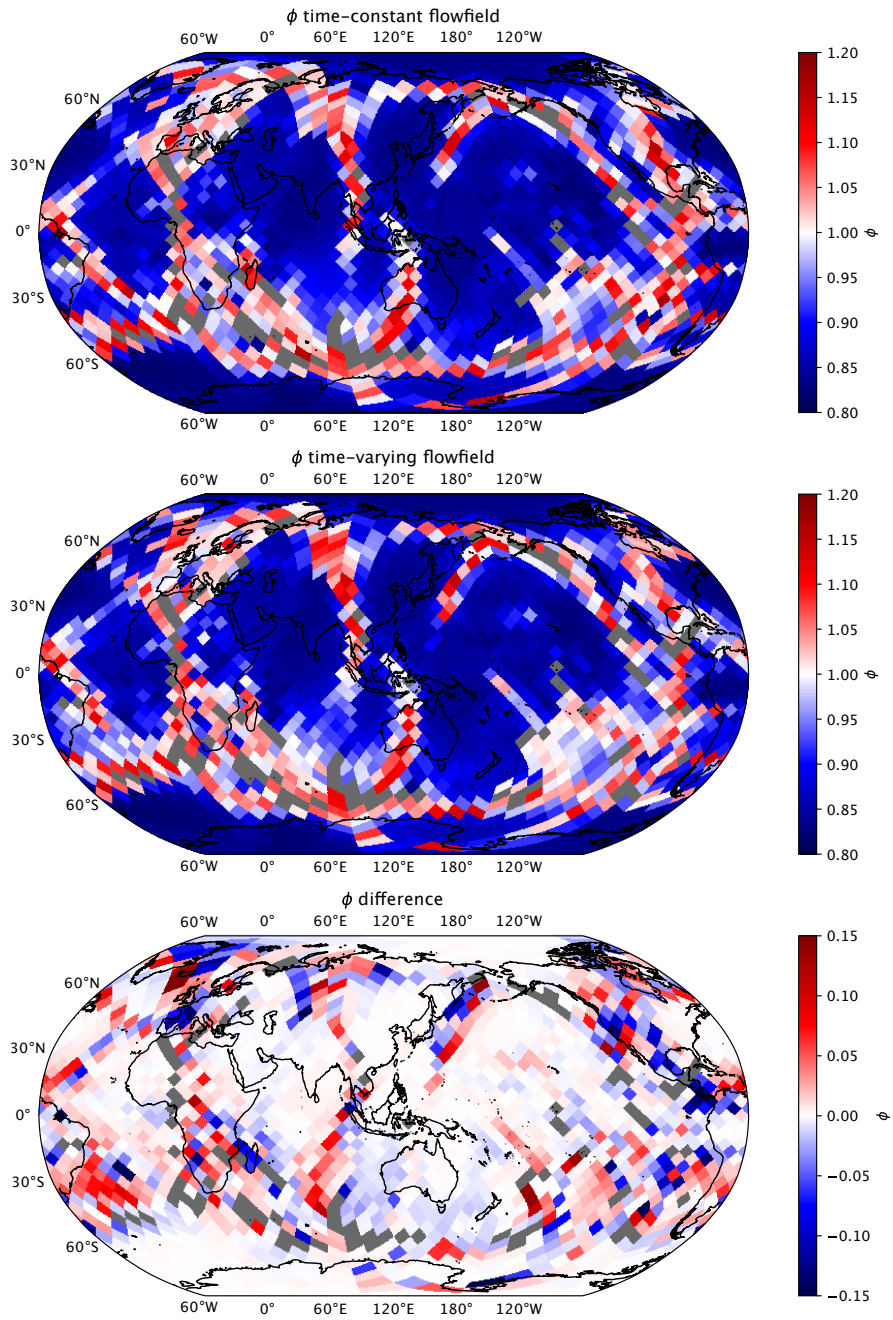


Figure A.15: Maps of P-wave radial anisotropy (ϕ) at 3530 km radius (50 km above the core–mantle boundary) for the easy-to-texture case. We show ϕ calculated with the time-constant flowfield (a), the time-varying flowfield (b) and the difference between the two (c).

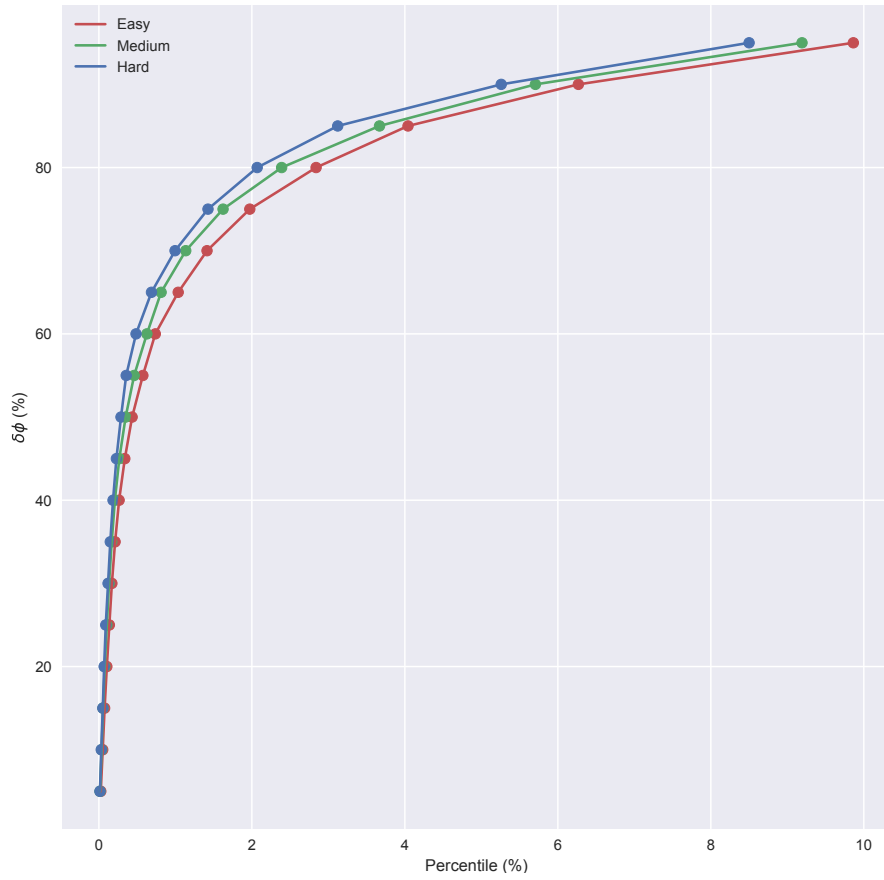


Figure A.16: The effect of slip system activities on the sensitivity of ξ observations to past flow in the lower mantle. This figure shows the different percentile ξ values coloured by the slip system label from Table 2. Notice at the larger percentiles the easy-to-texture case always has larger differences in ξ between the flow fields.

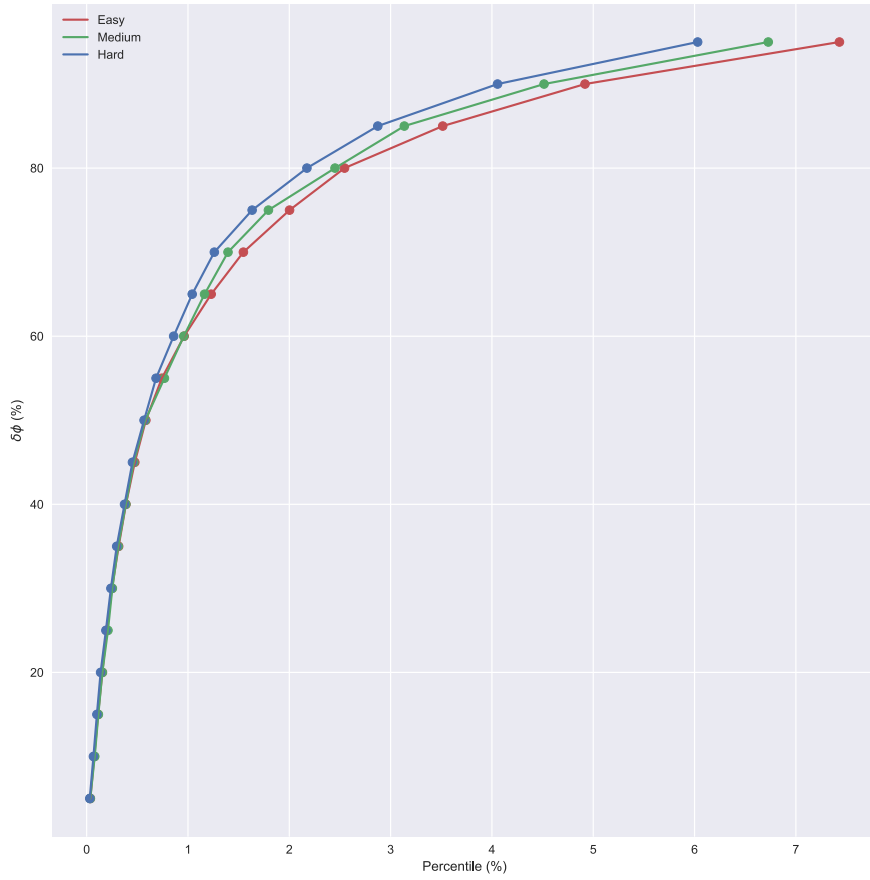


Figure A.17: The effect of slip system activities on the sensitivity of ϕ observations to past flow in the lower mantle. This figure shows the different percentile ϕ values coloured by the slip system label from Table 2. Notice at the larger percentiles the easy-to-texture case always has larger differences in ϕ between the flow fields.

516 **References**

- 517 Ammann, M., Brodholt, J., Wookey, J., Dobson, D., 2010. First-principles
518 constraints on diffusion in lower-mantle minerals and a weak D'' layer.
519 Nature 465, 462–465.
- 520 Asplet, J., Wookey, J., Kendall, M., 2020. A potential post-perovskite
521 province in D'' beneath the Eastern Pacific: evidence from new analysis
522 of discrepant SKS–SKKS shear wave splitting. Geophysical Journal
523 International 221, 2075–2090.
- 524 Auer, L., Boschi, L., Becker, T., Nissen-Meyer, T., Giardini, D., 2014. Savani:
525 A variable resolution whole-mantle model of anisotropic shear velocity variations
526 based on multiple data sets. Journal of Geophysical Research: Solid
527 Earth 119, 3006–3034.
- 528 Baumgardner, J.R., 1985. Three-dimensional treatment of convective
529 flow in the earth's mantle. Journal of Statistical Physics 39, 501–511.
530 doi:10.1007/BF01008348.
- 531 Boioli, F., Carrez, P., Cordier, P., Devincere, B., Gourié, K., Hirel, P.,
532 Kraych, A., Ritterbex, S., 2017. Pure climb creep mechanism drives flow
533 in Earth's lower mantle. Science Advances 3, e1601958.
- 534 Browaeys, J.T., Chevrot, S., 2004. Decomposition of the elastic tensor and
535 geophysical applications. Geophysical Journal International 159, 667–678.
- 536 Bunge, H.P., Richards, M.A., Baumgardner, J.R., 1997. A sensitivity study
537 of three-dimensional spherical mantle convection at 10⁸ Rayleigh number:
538 Effects of depth-dependent viscosity, heating mode, and an endothermic
539 phase change. Journal of Geophysical Research: Solid Earth 102, 11991–
540 12007. doi:10.1029/96JB03806. ISBN: 0148-0227.
- 541 Chandler, B.C., Chen, L.W., Li, M., Romanowicz, B., Wenk, H.R., 2021.
542 Seismic anisotropy, dominant slip systems and phase transitions in the
543 lowermost mantle. Geophysical Journal International 227, 1665–1681.
- 544 Chang, S.J., Ferreira, A.M., Ritsema, J., van Heijst, H.J., Woodhouse, J.H.,
545 2014. Global radially anisotropic mantle structure from multiple datasets:
546 a review, current challenges, and outlook. Tectonophysics 617, 1–19.

- 547 Cottaar, S., Li, M., McNamara, A.K., Romanowicz, B., Wenk, H.R., 2014.
548 Synthetic seismic anisotropy models within a slab impinging on the core-
549 mantle boundary. *Geophysical Journal International* 199, 164–177.
- 550 Cottaar, S., Romanowicz, B., 2013. Observations of changing anisotropy
551 across the southern margin of the African LLSVP. *Geophysical Journal*
552 *International* 195, 1184–1195.
- 553 Davies, D.R., Goes, S., Davies, J.H., Schuberth, B., Bunge, H.P., Ritsema, J.,
554 2012a. Reconciling dynamic and seismic models of Earth’s lower mantle:
555 The dominant role of thermal heterogeneity. *Earth and Planetary Science*
556 *Letters* 353, 253–269.
- 557 Davies, D.R., Goes, S., Davies, J.H., Schuberth, B.S.A., Bunge,
558 H.P., Ritsema, J., 2012b. Reconciling dynamic and seismic
559 models of Earth’s lower mantle: The dominant role of ther-
560 mal heterogeneity. *Earth and Planetary Science Letters* 353-354,
561 253–269. URL: <http://dx.doi.org/10.1016/j.epsl.2012.08.016>,
562 doi:10.1016/j.epsl.2012.08.016. publisher: Elsevier ISBN: 0012-821X.
- 563 Davies, J.H., Davies, D.R., 2010. Earth’s surface heat flux. *Solid Earth* 1,
564 5–24.
- 565 De Wit, R., Trampert, J., 2015. Robust constraints on average radial lower
566 mantle anisotropy and consequences for composition and texture. *Earth*
567 *and Planetary Science Letters* 429, 101–109.
- 568 Deschamps, F., Cobden, L., 2022. Estimating core-mantle boundary tem-
569 perature from seismic shear velocity and attenuation. *Frontiers in Earth*
570 *Science* 10, 1031507.
- 571 Dobson, D.P., Lindsay-Scott, A., Hunt, S.A., Bailey, E., Wood, I.G., Brod-
572 holt, J.P., Vocablo, L., Wheeler, J., 2019. Anisotropic diffusion creep in
573 postperovskite provides a new model for deformation at the core- mantle
574 boundary. *Proceedings of the National Academy of Sciences* 116, 26389–
575 26393.
- 576 Gorski, K.M., Hivon, E., Banday, A.J., Wandelt, B.D., Hansen, F.K., Rei-
577 necke, M., Bartelmann, M., 2005. HEALPix: A framework for high-
578 resolution discretization and fast analysis of data distributed on the sphere.
579 *The Astrophysical Journal* 622, 759.

- 580 Hansen, L., Zimmerman, M., Kohlstedt, D., 2012. Laboratory measurements
581 of the viscous anisotropy of olivine aggregates. *Nature* 492, 415–418.
- 582 van Heck, H.J., Davies, J.H., Elliott, T., Porcelli, D., 2016. Global-scale
583 modelling of melting and isotopic evolution of Earth’s mantle: Melting
584 modules for TERRA. *Geoscientific Model Development* 9, 1399–1411.
585 doi:10.5194/gmd-9-1399-2016.
- 586 Hirose, K., Wentzcovitch, R., Yuen, D., Lay, T., 2015. Mineralogy of the
587 deep mantle—The post-perovskite phase and its geophysical significance.
588 *Treatise on Geophysics* , 85–115.
- 589 Hunter, J.D., 2007. Matplotlib: A 2D graphics environment. *Computing in*
590 *Science & Engineering* 9, 90–95. doi:10.1109/MCSE.2007.55.
- 591 van Keken, P.E., Ballentine, C.J., 1998. Whole-mantle versus layered man-
592 tle convection and the role of a high-viscosity lower mantle in terres-
593 trial volatile evolution. *Earth and Planetary Science Letters* 156, 19–32.
594 doi:10.1016/s0012-821x(98)00023-5.
- 595 Kennett, B.L., Engdahl, E., Buland, R., 1995. Constraints on seismic veloci-
596 ties in the Earth from traveltimes. *Geophysical Journal International* 122,
597 108–124.
- 598 Kim, T., Ko, B., Greenberg, E., Prakapenka, V., Shim, S.H., Lee, Y., 2020.
599 Low melting temperature of anhydrous mantle materials at the core-mantle
600 boundary. *Geophysical Research Letters* 47, e2020GL089345.
- 601 Kuwayama, Y., Hirose, K., Cobden, L., Kusakabe, M., Tateno, S., Ohishi,
602 Y., 2022. Post-perovskite phase transition in the pyrolytic lowermost man-
603 tle: Implications for ubiquitous occurrence of post-perovskite above CMB.
604 *Geophysical Research Letters* 49, e2021GL096219.
- 605 Labrosse, S., Jaupart, C., 2007. Thermal evolution of the Earth : Secular
606 changes and fluctuations of plate characteristics. *Earth and Planetary*
607 *Science Letters* 260, 465–481. doi:10.1016/j.epsl.2007.05.046.
- 608 Lebensohn, R.A., Tomé, C., 1993. A self-consistent anisotropic approach for
609 the simulation of plastic deformation and texture development of polycrys-
610 tals: application to zirconium alloys. *Acta metallurgica et materialia* 41,
611 2611–2624.

- 612 Li, Y., Deschamps, F., Tackley, P.J., 2014. Effects of low-viscosity post-
613 perovskite on the stability and structure of primordial reservoirs in the
614 lower mantle. *Geophysical Research Letters* 41, 7089–7097.
- 615 Lobanov, S.S., Speziale, S., Brune, S., 2021. Modelling Mie scattering in
616 pyrolite in the laser-heated diamond anvil cell: Implications for the core-
617 mantle boundary temperature determination. *Physics of the Earth and
618 Planetary Interiors* 318, 106773.
- 619 Mameri, L., Tommasi, A., Signorelli, J., Hansen, L.N., 2019. Predicting
620 viscoplastic anisotropy in the upper mantle: a comparison between ex-
621 periments and polycrystal plasticity models. *Physics of the Earth and
622 Planetary Interiors* 286, 69–80.
- 623 McKenzie, D.P., Roberts, J.M., Weiss, N.O., 1974. Convection in the earth's
624 mantle: Towards a numerical simulation. *Journal of Fluid Mechanics* 62,
625 465–538. doi:10.1017/S0022112074000784. iSBN: 0022-1120.
- 626 McNamara, A.K., Karato, S.I., Van Keken, P.E., 2001. Localization of dis-
627 location creep in the lower mantle: implications for the origin of seismic
628 anisotropy. *Earth and Planetary Science Letters* 191, 85–99.
- 629 McNamara, A.K., van Keken, P.E., Karato, S.I., 2003. Development of fi-
630 nite strain in the convecting lower mantle and its implications for seismic
631 anisotropy. *Journal of Geophysical Research: Solid Earth* 108.
- 632 McNamara, A.K., Van Keken, P.E., Karato, S.I., 2002. Development of
633 anisotropic structure in the Earth's lower mantle by solid-state convection.
634 *Nature* 416, 310–314.
- 635 Merdith, A.S., Williams, S.E., Collins, A.S., Tetley, M.G., Mulder, J.A.,
636 Blades, M.L., Young, A., Armistead, S.E., Cannon, J., Zahirovic, S.,
637 Müller, R.D., 2020. Extending full-plate tectonic models into deep time:
638 Linking the neoproterozoic and the phanerozoic. *Earth-Science Reviews*
639 214, 103477. doi:10.1016/j.earscirev.2020.103477. publisher: Elsevier BV.
- 640 Merkel, S., McNamara, A.K., Kubo, A., Speziale, S., Miyagi, L., Meng,
641 Y., Duffy, T.S., Wenk, H.R., 2007. Deformation of (Mg,Fe)SiO₃ post-
642 perovskite and D'' anisotropy. *Science* 316, 1729–1732.

- 643 Met Office, 2010 - 2015. Cartopy: a cartographic python li-
644 brary with a Matplotlib interface. Exeter, Devon. URL:
645 <https://scitools.org.uk/cartopy>.
- 646 Miyagi, L., Kanitpanyacharoen, W., Kaercher, P., Lee, K.K., Wenk, H.R.,
647 2010. Slip systems in MgSiO₃ post-perovskite: Implications for D''
648 anisotropy. *Science* 329, 1639–1641.
- 649 Nowacki, A., Cottaar, S., 2021. Toward imaging flow at the base of the
650 mantle with seismic, mineral physics, and geodynamic constraints. *Mantle*
651 *Convection and Surface Expressions* , 329–352.
- 652 Nowacki, A., Walker, A.M., Wookey, J., Kendall, J.M., 2013. Evaluating
653 post-perovskite as a cause of D'' anisotropy in regions of palaeosubduction.
654 *Geophysical Journal International* 192, 1085–1090.
- 655 Nowacki, A., Wookey, J., J-Michael, K., 2010. Deformation of the lowermost
656 mantle from seismic anisotropy. *Nature* , 1091–1094.
- 657 Nowacki, A., Wookey, J., Kendall, J.M., 2011. New advances in us-
658 ing seismic anisotropy, mineral physics and geodynamics to under-
659 stand deformation in the lowermost mantle. *Journal of Geodynamics*
660 52, 205–228. URL: <http://dx.doi.org/10.1016/j.jog.2011.04.003>,
661 doi:10.1016/j.jog.2011.04.003.
- 662 Panton, J., Davies, J.H., Myhill, R., 2023. The Stability of Dense Oceanic
663 Crust Near the Core-Mantle Boundary. *Journal of Geophysical Research:*
664 *Solid Earth* 128, e2022JB025610. doi:10.1029/2022JB025610.
- 665 Park, Y., Azuma, S., Okazaki, K., Uesugi, K., Yasutake, M., Nishihara,
666 Y., Nomura, R., 2022. Development of Lattice-Preferred Orientations of
667 MgO Periclase From Strain Rate Controlled Shear Deformation Experi-
668 ments Under Pressure up to 120 GPa. *Geophysical Research Letters* 49,
669 e2022GL100178.
- 670 Reali, R., Van Orman, J.A., Pigott, J.S., Jackson, J.M., Boioli, F., Carrez,
671 P., Cordier, P., 2019. The role of diffusion-driven pure climb creep on the
672 rheology of bridgmanite under lower mantle conditions. *Scientific Reports*
673 9, 2053.

- 674 Restelli, F., Koelemeijer, P., Ferreira, A., 2023. Normal mode observability of
675 radial anisotropy in the Earth's mantle. *Geophysical Journal International*
676 233, 663–679.
- 677 Silver, P.G., Chan, W.W., 1991. Shear wave splitting and subcontinental
678 mantle deformation. *Journal of Geophysical Research: Solid Earth* 96,
679 16429–16454.
- 680 Simmons, N., Myers, S., Morency, C., Chiang, A., Knapp, D., 2021. SPiRaL:
681 a multiresolution global tomography model of seismic wave speeds and
682 radial anisotropy variations in the crust and mantle. *Geophysical Journal*
683 *International* 227, 1366–1391.
- 684 Stackhouse, S., Brodholt, J.P., 2007. The high-temperature elasticity of
685 MgSiO₃ post-perovskite. Washington DC American Geophysical Union
686 *Geophysical Monograph Series* 174, 99–113.
- 687 Stackhouse, S., Brodholt, J.P., Wookey, J., Kendall, J.M., Price, G.D., 2005.
688 The effect of temperature on the seismic anisotropy of the perovskite and
689 post-perovskite polymorphs of MgSiO₃. *Earth and Planetary Science Let-*
690 *ters* 230, 1–10.
- 691 Walker, A., Forte, A., Wookey, J., Nowacki, A., Kendall, J.M., 2011. Elastic
692 anisotropy of D'' predicted from global models of mantle flow. *Geochem-*
693 *istry, Geophysics, Geosystems* 12.
- 694 Walker, A.M., Dobson, D.P., Wookey, J., Nowacki, A., Forte, A.M., 2018.
695 The anisotropic signal of topotaxy during phase transitions in D''. *Physics*
696 *of the Earth and Planetary Interiors* 276, 159–171.
- 697 Wenk, H.R., Cottar, S., Tomé, C.N., McNamara, A., Romanowicz, B., 2011.
698 Deformation in the lowermost mantle: From polycrystal plasticity to seis-
699 mic anisotropy. *Earth and Planetary Science Letters* 306, 33–45.
- 700 Wenk, H.R., Speziale, S., McNamara, A., Garnero, E., 2006. Modeling lower
701 mantle anisotropy development in a subducting slab. *Earth and Planetary*
702 *Science Letters* 245, 302–314.
- 703 Wentzcovitch, R.M., Tsuchiya, T., Tsuchiya, J., 2006. MgSiO₃ postper-
704 ovskite at D'' conditions. *Proceedings of the National Academy of Sciences*
705 103, 543–546.

- 706 Wheeler, J., 2009. The preservation of seismic anisotropy in the Earth's man-
707 tle during diffusion creep. *Geophysical Journal International* 178, 1723–
708 1732.
- 709 Wolf, J., Frost, D.A., Long, M.D., Garnero, E., Aderoju, A.O., Creasy, N.,
710 Bozdağ, E., 2023a. Observations of mantle seismic anisotropy using array
711 techniques: Shear-wave splitting of beamformed SmKS phases. *Journal of*
712 *Geophysical Research: Solid Earth* 128, e2022JB025556.
- 713 Wolf, J., Long, M.D., Li, M., Garnero, E., 2023b. Global compilation of deep
714 mantle anisotropy observations and possible correlation with low velocity
715 provinces. *Geochemistry, Geophysics, Geosystems* 24, e2023GC011070.
- 716 Wookey, J., Kendall, J.M., Rumpker, G., 2005. Lowermost mantle anisotropy
717 beneath the north Pacific from differential S—ScS splitting. *Geophysical*
718 *Journal International* 161, 829–838.